



# Quantifying the Impact of the Dust Torque on the Migration of Low-mass Planets

Octavio M. Guilera<sup>1,2</sup> , Pablo Benitez-Llambay<sup>3</sup> , Marcelo M. Miller Bertolami<sup>1</sup> , and Martin E. Pessah<sup>4,5</sup> <sup>1</sup>Instituto de Astrofísica de La Plata (IALP), CCT La Plata-CONICET-UNLP, Paseo del Bosque s/n, La Plata, Argentina; [oguilera@fcaglp.unlp.edu.ar](mailto:oguilera@fcaglp.unlp.edu.ar)<sup>2</sup>Núcleo Milenio de Formación Planetaria (NPF), Chile<sup>3</sup>Facultad de Ingeniería y Ciencias, Universidad Adolfo Ibáñez, Av. Diagonal las Torres 2640, Peñalolén, Chile<sup>4</sup>Niels Bohr International Academy, Niels Bohr Institute, Blegdamsvej 17, DK-2100 Copenhagen Ø, Denmark<sup>5</sup>School of Natural Sciences, Institute for Advanced Study, 1 Einstein Drive, Princeton, NJ 08540, USA

Received 2023 January 18; revised 2023 April 20; accepted 2023 May 3; published 2023 August 7

## Abstract

Disk solids are critical in many planet formation processes; however, their effect on planet migration remains largely unexplored. Here we assess this important issue for the first time by building on the systematic measurements of dust torques on an embedded planet by Benitez-Llambay & Pessah. Adopting standard models for the gaseous disk and its solid content, we quantify the impact of the dust torque for a wide range of conditions describing the disk/planet system. We show that the total torque can be positive and reverse inward planet migration for planetary cores with  $M_p \lesssim 10 M_\oplus$ . We compute formation tracks for low-mass embryos for conditions usually invoked when modeling planet formation processes. Our most important conclusion is that dust torques can have a significant impact on the migration and formation history of planetary embryos. The most important implications of our findings are as follows. (i) For nominal dust-to-gas mass ratios  $\epsilon \simeq 0.01$ , low-mass planets migrate outwards beyond the water ice-line if most of the mass in the solids is in particles with Stokes numbers  $St \simeq 0.1$ . (ii) For  $\epsilon \gtrsim 0.02\text{--}0.05$ , solids with small Stokes numbers,  $St \simeq 0.01$ , can play a dominant role if most of the mass is in those particles. (iii) Dust torques have the potential to enable low-mass planetary cores formed in the inner disk to migrate outwards and act as the seed for massive planets at distances of tens of au.

*Unified Astronomy Thesaurus concepts:* [Protoplanetary disks \(1300\)](#); [Planetary-disk interactions \(2204\)](#); [Planet formation \(1241\)](#); [Planetary migration \(2206\)](#)

## 1. Introduction

As planets grow and evolve in the protoplanetary disks where they form, they modify the environment surrounding them, which in turn can alter the planet's evolution. In particular, a planet embedded in a disk leads to asymmetric structures with the ability to exert a net torque on the planet that can alter its dynamics. The ensuing planet migration is a key process in planet formation (see Venturini et al. 2020c, and references therein). While the presence of disk solids is widely recognized as critical in many processes involved in planet formation and evolution, their role has not been assessed in planet migration. Building on the first systematic measurements of dust torques on an embedded planet reported by Benítez-Llambay & Pessah (2018, hereafter BLP18), this paper is a first attempt to address this important issue.

In sufficiently viscous disks, the gas torque exerted onto the planet has two important contributions: the differential Lindblad torque and the corotation torque. The former is negative for typical protoplanetary disk models, while the latter depends sensitively on the vortensity/entropy gradients within the planet's corotation region. For low-mass planets,  $M_p \lesssim 10 M_\oplus$ , these two components of the gas torque are of the same order of magnitude but have opposite signs, leading to the so-called type I migration regime (e.g., Tanaka et al. 2002). Positive corotation torques can dominate over the differential Lindblad torque locally so that a planet migrates outwards transiently (e.g., Dittkrist et al. 2014; Baillié et al. 2016;

Guilera et al. 2017). However, overall, planets tend to experience fast inward migration on a global scale. This makes it challenging to explain the existence of giant planets at moderate to large distances from the central star (e.g., Miguel et al. 2011; Ronco et al. 2017; Voelkel et al. 2022). If planetary cores of the order of  $10 M_\oplus$  can hover around these regions while there is still sufficient gas in the disk, this may lend a possible way to form giant planets at these locations.

In order to alleviate the fast inward migration problem, different mechanisms have been proposed to slow down—or even reverse—the migration of growing planets. Most of these focus on thermodynamic effects in nonisothermal disks or modifications of temperature/entropy and gas density gradients close to the planet (see Paardekooper et al. 2022, for a recent review, and references therein). In addition, Guilera & Sándor (2017) and Guilera et al. (2020) showed that pressure maxima induced by a viscosity transition in the disk can act as a migration trap for growing planets. Moreover, Benítez-Llambay et al. (2015) showed that the luminosity of an accreting planet is able to asymmetrically modify the temperature/density close to the planet in such a way that an additional “heating torque” develops. The heating torque is always positive and can slow down or even reverse the planet's migration. More recently, Guilera et al. (2019, 2021) incorporated this effect into a global model of planet formation, showing that heating torques can generate significant outward migration for planets growing by pebble accretion.

Given the fact that protoplanetary disks are made of gas and a small fraction of solids—elements condensed as grains or dust—it is relevant to consider the possibility that gravitational torques exerted by solids can affect planet migration. Perhaps

because solids are thought to contribute only about 1% of the total mass of the protoplanetary disk, there have only been a handful of studies about the exchange of angular momentum between the planets and the solid component of the disk (e.g., Capobianco et al. 2011; Chrenko 2017; Benítez-Llambay & Pessah 2018; Chen & Lin 2018; Kanagawa 2019; Pierens et al. 2019; Hsieh & Lin 2020; Regály 2020). In particular, the 2D hydrodynamical simulations from BLP18 show that for low- to intermediate-mass planets, an asymmetric dust density distribution develops and exerts a net torque onto the planet. This “dust torque” is generally positive, and its value depends on the Stokes number of solids, the dust-to-gas mass ratio, and the planet mass. It can be of the order of (or much larger than) the gas torque and locally slow down, halt, or reverse planet migration for planetary cores with  $M_p \lesssim 10 M_\oplus$ . It is then imperative to consider the cumulative effect of the dust torque when integrating the equations of motion of the embedded forming planets.

The aim of this work is to build on the torque measurements provided by BLP18 and investigate the global dynamics of low-mass planetary cores embedded in dusty disks in order to quantify the impact of the dust torque on their migration and formation history. The rest of the paper is organized as follows. In Section 2, we present the scope of our framework for computing the torque exerted on a planet embedded in a gaseous disk that can contain a dust component. Subsequently, we compute torque maps, characterizing the dependence of the total torque on a planet on the various physical parameters describing the planet–disk system and/or the dust component. These include the planet’s location, the dust-to-gas mass ratio, the stellar mass accretion rate, and the dust Stokes number distribution. We present the results for steady-state locally isothermal (with a radial temperature gradient) and nonisothermal (with radial and vertical thermal structure) disks in Sections 3 and 4, respectively. Based on these torque maps, in Section 5, we compute for the first time the formation tracks of low-mass planets embedded in dusty disks where the torque exerted by the dust component is considered. This allows us to quantify the role of dust in low-mass planetary migration considering a range of solid accretion rates on single planets embedded in both steady-state and evolving disks. In Section 6, we outline the implications of our findings, together with the most important present caveats and possible directions to address them. Finally, in Section 7, we summarize the most important takeaways and conclusions from this first study.

## 2. Framework for Computing Planetary Torques

Computing the torque exerted on an embedded planet by the gas and dust component in a protoplanetary disk requires solving the associated multispecies hydrodynamic equations for a particular disk model, planetary mass, and dust size distribution. This is, in all generality, a daunting task. Here we approach this problem in a simplified way by considering existing models for the gas torque responsible for type I migration (Tanaka et al. 2002; Jiménez & Masset 2017) together with the measurements of the dust-to-gas torque ratio provided by BLP18 obtained for a wide range of planetary masses and dust Stokes numbers for a single planet embedded in a standard  $\alpha$ -disk model in a steady state.

### 2.1. Torque Calculation

We consider the total torque,  $\Gamma_{\text{tot}}$ , acting on a planet as given by<sup>6</sup>

$$\Gamma_{\text{tot}} = \Gamma_g + \Gamma_d, \quad (1)$$

where  $\Gamma_g$  and  $\Gamma_d$  are the torques exerted by the gas and dust, respectively. For a given disk model, these torques are obtained as described below.

#### 2.1.1. Gas Torque

For the locally isothermal disks discussed in Section 3, we employ the gas torque model associated with type I migration as derived by Tanaka et al. (2002) assuming a globally isothermal disk with a power-law density profile

$$\Gamma_g = - \left[ 1.364 - 0.54 \left( \frac{d \ln \Sigma_g}{d \ln r} \right) \right] \Gamma_p. \quad (2)$$

Here  $\Gamma_g$  is the sum of the differential Lindblad and corotation torques, and  $\Gamma_p$  stands for the reference torque evaluated at the radial location of the planet  $r_p$  as given by

$$\Gamma_p = q^2 h_p^{-2} \Sigma_{g,p} r_p^4 \Omega_{K,p}^2, \quad (3)$$

with  $\Sigma_g$  the gas surface density,  $q = M_p/M_\star$  the planet-to-star mass ratio, and  $h = c_s/(r\Omega_K)$  the disk aspect ratio. Here  $c_s$  is the sound speed, and  $\Omega_K = \sqrt{GM_\star/r^3}$  is the Keplerian frequency. The subscript “p” indicates quantities being evaluated at  $r = r_p$ .

Using Equation (2) to compute the gas torque for disks with radial temperature gradients is, of course, an approximation, but this enables us to capture the characteristic dependencies of type I migration with the underlying disk model in a simple way. Note that, under the stated assumptions,  $\Gamma_p$  encapsulates all of the radial dependencies of the physical parameters characterizing the gas torque in a dust-free disk.

For the nonisothermal disk models (i.e., with vertical thermal structure) presented in Section 4, we employ the gas torque models responsible for type I migration derived by Jiménez & Masset (2017). The gas torque  $\Gamma_g$  we consider is then again the sum of the differential Lindblad and corotation torques and also proportional to  $\Gamma_p$ , defined in Equation (3). In this case, the differential Lindblad torque depends mainly on the local gradients of the gas surface density and midplane temperature, while the corotation torque has four contributions, three of them associated with the disk radial gradients of vortensity, entropy, and temperature and a fourth one accounting for the viscous production of vortensity; see Jiménez & Masset (2017) and Equations (26)–(28) and (A.10)–(A.23) in Guilera et al. (2019).<sup>7</sup>

#### 2.1.2. Dust Torque

If the dust-to-gas mass ratio  $\epsilon$  is small, we can neglect the dust back-reaction force onto the gas, and  $\Gamma_d$  scales linearly<sup>8</sup>

<sup>6</sup> For simplicity, in this first study, we do not include the so-called thermal torque (as in Guilera et al. 2021) that could lead to either outward or faster inward migration (Masset 2017).

<sup>7</sup> We note that what we define as  $\Gamma_p$  in Equation (3) in this work is defined as  $\Gamma_0$  in Guilera et al. (2019, Equation (21)) and BLP18.

<sup>8</sup> For a small enough total dust-to-gas mass ratio, the linear scaling holds for each individual dust species.

**Table 1**  
Values for  $\Gamma_d/\Gamma_0$  and  $\Gamma_g/\Gamma_0$  Provided in BLP18 (See Their Figure 2)

$M_p/M_\oplus$	0.333	0.486	0.709	1.03	1.51	2.2	3.22	4.69	6.85	10.0
St										
0.010	0.283	0.309	0.264	0.201	0.142	0.093	0.056	0.029	0.006	-0.010
0.014	0.371	0.394	0.415	0.333	0.239	0.160	0.098	0.053	0.017	-0.008
0.021	0.739	0.720	0.618	0.475	0.382	0.276	0.172	0.095	0.041	-0.002
0.030	1.638	1.332	1.102	0.851	0.625	0.434	0.275	0.185	0.087	0.021
0.043	3.254	2.614	1.961	1.476	1.078	0.757	0.503	0.316	0.174	0.085
0.062	5.776	4.579	3.428	2.461	1.790	1.266	0.850	0.546	0.326	0.167
0.089	9.672	7.297	5.313	3.760	2.620	1.872	1.301	0.880	0.562	0.304
0.127	13.684	10.191	7.337	5.145	3.471	2.374	1.725	1.209	0.805	0.483
0.183	16.058	11.276	7.866	5.231	3.178	1.372	1.740	1.493	1.073	0.701
0.264	-1.521	-18.135	-8.446	-0.425	1.971	1.746	2.237	1.823	1.351	0.910
0.379	-32.124	-7.348	2.307	4.517	4.752	3.232	2.803	2.108	1.499	1.016
0.546	5.523	8.831	9.054	7.882	5.860	3.741	2.716	1.953	1.398	0.986
0.785	10.492	9.803	7.187	5.859	4.314	3.278	2.465	1.821	1.326	0.943
1.129	11.861	9.572	7.850	5.807	4.538	3.367	2.463	1.799	1.299	0.916
$\Gamma_g/\Gamma_0$	-3.57	-3.42	-3.25	-3.05	-2.82	-2.55	-2.25	-1.95	-1.68	-1.50

**Note.** Values obtained for a reference radius  $r_0 = 1$  au and dust-to-gas mass ratio  $\epsilon_0 = 0.01$ .

with  $\epsilon$ , i.e.,

$$\Gamma_d(r_p, \epsilon) = \frac{\epsilon}{\epsilon_0} \times \Gamma_d(r_p, \epsilon_0). \quad (4)$$

We furthermore assume that, similarly to the models for the gas torque,<sup>9</sup> the dust torque (for a given dust-to-gas mass ratio) is proportional to the reference torque, i.e.,

$$\Gamma_d(r_p, \epsilon_0) = \frac{\Gamma_p}{\Gamma_0} \times \Gamma_d(r_0, \epsilon_0), \quad (5)$$

where  $\Gamma_p$  and  $\Gamma_0$  stand for the reference torque in Equation (3) evaluated at the location of the planet  $r_p$  and at the reference location  $r = r_0$ , respectively. Combining Equations (4) and (5), the dust torque can be written as

$$\Gamma_d(r_p, \epsilon) = \frac{\epsilon}{\epsilon_0} \times \frac{\Gamma_d(r_0, \epsilon_0)}{\Gamma_0} \times \Gamma_p. \quad (6)$$

The value of the ratio  $\Gamma_d(r_0, \epsilon_0)/\Gamma_0$  is obtained from BLP18, where  $r_0 = 1$  au and  $\epsilon_0 = 0.01$  (see their Figure 2). The dust torque can then be finally expressed as

$$\Gamma_d = \left( \frac{\epsilon}{0.01} \right) \left( \frac{\Gamma_d}{\Gamma_0} \right)_{\text{BLP18}} \Gamma_p, \quad (7)$$

where  $(\Gamma_d/\Gamma_0)_{\text{BLP18}}$  is the dust torque measured from numerical simulations in BLP18. These values are listed in Table 1 for logarithmically spaced planetary masses and Stokes numbers, St, in the range  $0.1 \leq M_p/M_\oplus \leq 10$  and  $10^{-2} \leq \text{St} \leq 1$ , respectively.

To obtain values of  $\Gamma_d$  for planetary masses and Stokes numbers that are not tabulated, we use bilinear interpolation in logarithmic space. In Figure 1, we show the interpolated dust torques from Table 1, which have been calculated considering  $r_p = r_0 = 1$  au and  $\epsilon = \epsilon_0 = 0.01$ .

In order to use Equation (7) to model planets migrating and growing in disks with more complex structure, we implicitly

assume that  $\Gamma_d$  does not depend strongly on the gas dynamics or the state of motion of the planet. We note here that the dust torque is expected to be more sensitive to the disk dynamics for small Stokes numbers, for which the dust torque decreases. Also, the dust torque could be sensitive to the state of motion of the planet if the relative drift between the solids and the planet is highly affected. This could happen, for example, if migration is very fast (with respect to the radial drift). We also note that the accretion of dust, i.e., the removal of solids inside the planetary Hill sphere, can affect the magnitude of the dust torque (e.g., Regály 2020). The validity and robustness of these hypotheses need to be assessed through dedicated hydrodynamical studies.

### 3. Locally Isothermal $\alpha$ -Disks

We first consider a steady-state, locally isothermal  $\alpha$ -disk model (Shakura & Sunyaev 1973) with a dust component characterized by a constant Stokes number throughout the disk as used by BLP18 and described in Weber et al. (2018). The  $\alpha$ -parameter relates the accretion rate to the gaseous disk surface density via

$$\Sigma_g = \frac{\dot{M}_*}{3\pi\nu}, \quad (8)$$

where  $\dot{M}_*$  is the mass accretion rate onto the central star,  $\nu = \alpha c_s h$  is the disk viscosity, and the aspect ratio,  $h$ , is considered to be constant. Under these assumptions, the background gas surface density and temperature are power laws in radius, with

$$\left. \frac{d \ln \Sigma_g}{d \ln r} \right|_{\text{isoth.}} = -\frac{1}{2} \quad \text{and} \quad \left. \frac{d \ln T}{d \ln r} \right|_{\text{isoth.}} = -1. \quad (9)$$

#### 3.1. Torque Maps for Fiducial Isothermal Disk Model

In what follows, we will employ the term ‘‘torque map’’ to characterize the dependence of the total torque  $\Gamma_{\text{tot}}$  on the various physical parameters describing the planet–disk system and/or the dust component. It is convenient to present

<sup>9</sup> We note that the ratio  $\Gamma_d/\Gamma_p$  may have an additional dependence with  $h$ , which we assume to be weak enough to be neglected. Testing the validity of this hypothesis requires dedicated hydrodynamical simulations that are beyond the scope of this paper.

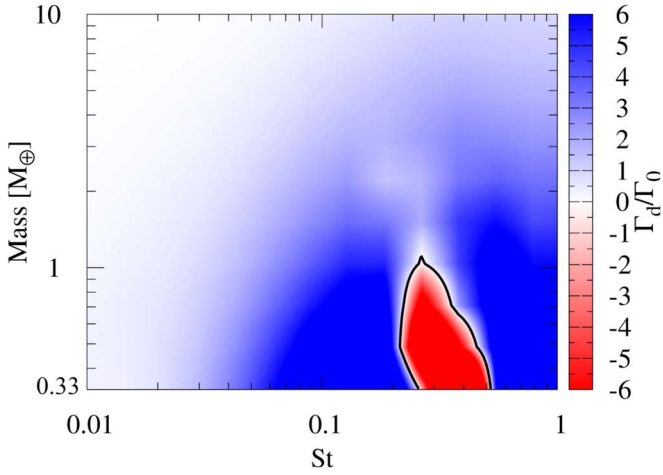


**Figure 1.** Normalized reference dust torque,  $\Gamma_d/\Gamma_0$ , for a range of planet masses and Stokes numbers for a vertically isothermal disk as obtained from the simulations in BLP18, with  $r_p = r_0 = 1$  au and  $\epsilon = \epsilon_0 = 0.01$ . The values shown correspond to the bilinear interpolation of data in Table 1.

normalized values  $\Gamma_{\text{tot}}/\Gamma_p$  using the reference torque  $\Gamma_p$ , defined in Equation (3).

In order to understand the scales involved in the problem at hand and build intuition before considering more elaborate models, we first consider dusty disk models similar to those in BLP18. These correspond to steady-state, vertically isothermal  $\alpha$ -disks with a constant aspect ratio  $h = 0.05$  around a central star of  $1 M_\odot$  with  $\dot{M}_* = 10^{-7} M_\odot \text{ yr}^{-1}$  and  $\alpha = 3 \times 10^{-3}$ . When the dust component is present, we set its constant gas-to-dust mass ratio to  $\epsilon = 0.01$ .

The normalized torque map  $\Gamma_{\text{tot}}/\Gamma_p$  as a function of planet mass and Stokes number, computed at 1 au for the isothermal disk model considered, is shown in Figure 2. The regions of the torque map corresponding to negative/positive values are associated with inward/outward migration. The two distinct regimes identified by BLP18 are evident: the gas-dominated regime for Stokes numbers  $St \simeq 0.05\text{--}0.2$  and planet masses  $M_p \lesssim 3 M_\oplus$  and the gravity-dominated regime for  $St \gtrsim 0.3\text{--}0.5$  and planet masses  $M_p \lesssim 7 M_\oplus$ .

In the gas-dominated regime (low values of  $St$ ), the torque increases with the Stokes number, allowing the outward migration of more massive planets as the Stokes number increases (up to a mass of  $3 M_\oplus$  at  $St \simeq 0.1$ ). On the other hand, in the gravity-dominated regime, the total torque is less sensitive to the value of the Stokes number, and the maximum mass for outward migration stays at about  $M_p \simeq 5\text{--}6 M_\oplus$ . In between these two regimes there exists a transition region ( $St \simeq 0.2\text{--}0.5$ ) where the intensity of the dust torque is strongly reduced and can even change sign, resulting mostly in inward migration. The total torque in this transition regime can depend sensitively on the mass of the planet. For the standard value of the dust-to-gas mass ratio considered here,  $\epsilon = 0.01$ , the total torque is practically equal to the gas torque for low Stokes numbers ( $St \lesssim 0.02$ ). However, as we will show in Section 4.2, this situation can drastically change if the dust-to-gas mass ratio increases.

The normalized torque map  $\Gamma_{\text{tot}}/\Gamma_p$  as a function of planet mass and disk location associated with our fiducial disk model is shown in Figure 3. The leftmost panel corresponds to a dust-free disk, whereas the subsequent panels show the results for dusty disks with three different (constant) Stokes numbers  $St = \{0.1, 0.3, 1\}$ .

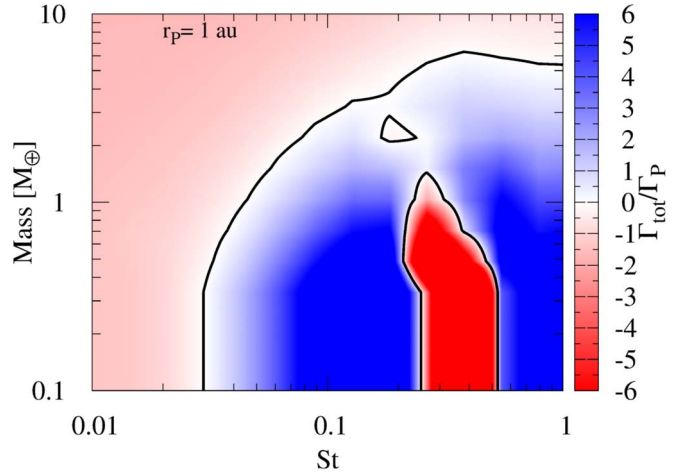


**Figure 2.** Normalized torque map,  $\Gamma_{\text{tot}}/\Gamma_p$ , for a range of planet masses and Stokes numbers at 1 au for a vertically isothermal disk. The color scale accentuates the regions where the total torque changes sign. Red/blue tones indicate negative/positive total torque, which locally implies inward/outward planet migration.

For the dust-free disk,  $\Gamma_{\text{tot}} = \Gamma_g$ , and  $\Gamma_{\text{tot}}/\Gamma_p$  is, by construction, constant with  $\Gamma_{\text{tot}}/\Gamma_p = -1.634$ . In the cases corresponding to  $St = 0.1$  and 1, the dust torque generates a significant region of positive total torque, shown in blue. For  $St = 0.1$ , this positive total torque region extends up to  $\simeq 3 M_\oplus$ , while for the case of  $St = 1$ , the positive total torque region extends up to  $\simeq 5 M_\oplus$ . The situation is quite different for the case of  $St = 0.3$ , where outward migration only ensues for masses  $1 M_\oplus \lesssim M_p \lesssim 6 M_\oplus$  and becomes inwards outside that range.

Note that for the isothermal disk model under consideration, all radial dependencies are encapsulated in  $\Gamma_p$ , and the value of the total torque depends only on the mass of the planet and not its location. Furthermore, because the disk aspect ratio is known, in this case  $h = 0.05$ ,  $\Gamma_p$  can be directly computed given the planet mass and location, and the total torque can be easily reconstructed from the color-magnitude of the maps. In the next section, we will see that for nonisothermal disks (where the disk aspect ratio  $h$  is no longer constant), the transition between positive and negative total torques depends on the planet location, with implications for its migration history.

Having gained some insight into the relative contribution of the dust torque in the framework of the isothermal  $\alpha$ -disk, we next consider a more realistic disk model.

#### 4. Nonisothermal $\alpha$ -Disks

We consider a steady-state, nonisothermal, axisymmetric  $\alpha$ -disk with radial and vertical thermal structure. The disk model is obtained by solving the classical structure and transport equations in the vertical direction, considering that vertical hydrostatic equilibrium at each radius results from viscous heating and irradiation from the central star.<sup>10</sup> Specifically, in order to compute the vertical structure of the disk, for a given  $\alpha$ -viscosity parameter and stellar mass accretion rate  $\dot{M}_*$ , we solve at each radial location the set of equations

$$\frac{\partial P}{\partial z} = -\rho \Omega^2 z, \quad (10)$$

<sup>10</sup> We used  $T_{\text{eff}} = 4397$  K and  $R_* = 3.079 R_\odot$  for a protostar of  $1 M_\odot$  as provided in Baraffe et al. (2015).

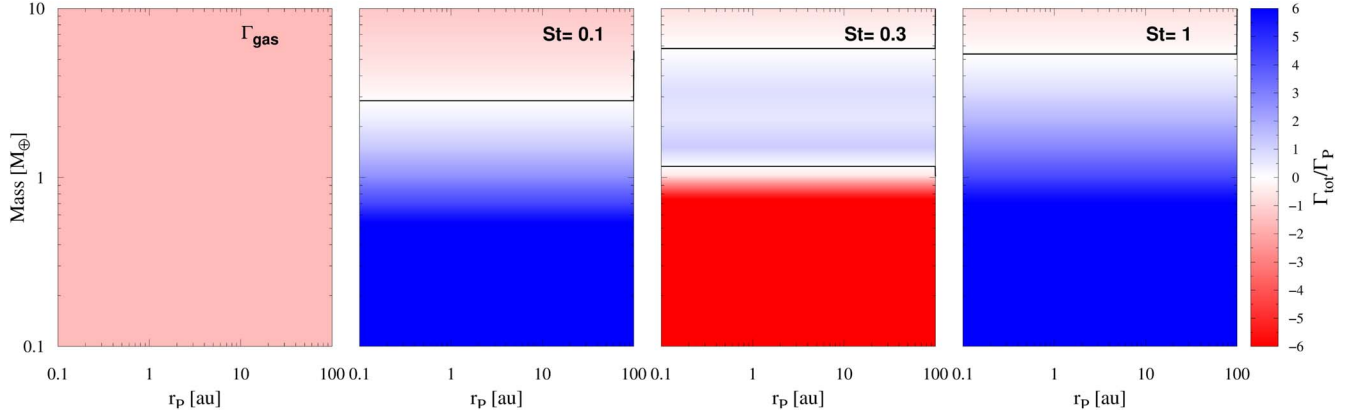


**Figure 3.** Normalized torque maps,  $\Gamma_{\text{tot}}/\Gamma_p$ , for a range of planet masses and locations in an isothermal disk. The left panel corresponds to a dust-free disk, whereas the other panels illustrate the results for a disk with a dust-to-gas mass ratio  $\epsilon = 0.01$  and particles with constant Stokes number  $\text{St} = \{0.1, 0.3, 1\}$ . Since for isothermal  $\alpha$ -disks, all of the radial dependencies of the torque are encapsulated in  $\Gamma_p$ , the normalized torques do not depend on the planet’s location.

$$\frac{\partial F}{\partial z} = \frac{9}{4} \rho \nu \Omega^2, \quad (11)$$

$$\frac{\partial T}{\partial z} = \nabla \frac{T}{P} \frac{\partial P}{\partial z}, \quad (12)$$

where  $P$ ,  $\rho$ ,  $\Omega$ ,  $T$ ,  $F$ , and  $z$  are the pressure, density, angular frequency, temperature, heat flux, and vertical distance from the disk midplane, respectively, and  $\nabla = d \ln T / d \ln P$  (see Guilera et al. 2017, 2019, for further details).

The logarithmic gradients for the gas surface density and midplane temperature, as well as the disk aspect ratio  $h$ , for a nonisothermal disk with  $\alpha = 3 \times 10^{-3}$  and  $\dot{M}_* = 10^{-7} M_\odot \text{ yr}^{-1}$  are shown in Figure 4. The (constant) values corresponding to the isothermal disk model are shown with dashed lines in the same figure for comparison. It is evident that the radial structure of the nonisothermal disk model cannot be described by a unique power law. In these models, heat transport and, in particular, radiative opacities play a key role in determining the density and midplane temperature profiles of the disk. The nontrivial radial disk structure may lead to noticeable differences between the nonisothermal and isothermal gas torque maps. However, in order to obtain the dust torque for the nonisothermal disk, we assume that the dust torque can still be computed using Equation (7), where the nonisothermal disk aspect ratio is used when computing the reference torque  $\Gamma_p$ .

The normalized torque map  $\Gamma_{\text{tot}}/\Gamma_p$  as a function of planet mass and Stokes number, computed at 1 au for the nonisothermal disk with a dust-to-gas mass ratio  $\epsilon = 0.01$ , is shown in Figure 5. As in the case of the isothermal disk model, the two regions of positive total torque, as well as the transition between these at  $\text{St} \simeq 0.2\text{--}0.5$ , are clearly visible. Similarly to the vertically isothermal disk, the dust torque does not play a relevant role for the standard dust-to-gas mass ratio of  $\epsilon_0 = 0.01$  when dust particles with low Stokes numbers, e.g.,  $\text{St} \lesssim 0.02$ , are considered. All of these features in the torque maps evaluated at 1 au, as seen in Figure 5, are also broadly present in these torque maps when calculated at other disk locations. However, due to the radial disk structure seen in Figure 4, the value of  $\Gamma_{\text{tot}}/\Gamma_p$  does depend on the planet’s location, in contrast to the isothermal disk case.

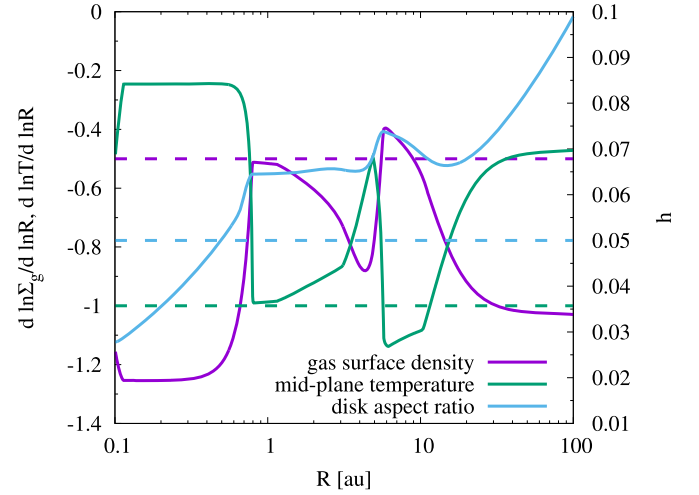


**Figure 4.** Radial profiles of the logarithmic gas surface density and midplane temperature gradients and the disk aspect ratio for the steady-state solution of an  $\alpha$ -disk considering  $\dot{M}_* = 10^{-7} M_\odot \text{ yr}^{-1}$  and  $\alpha = 3 \times 10^{-3}$ . The solid lines correspond to the nonisothermal disk, while the dashed ones illustrate the isothermal disk case. The abrupt changes in the midplane temperature and gas surface density gradients are due to sharp disk opacity transitions at such locations.

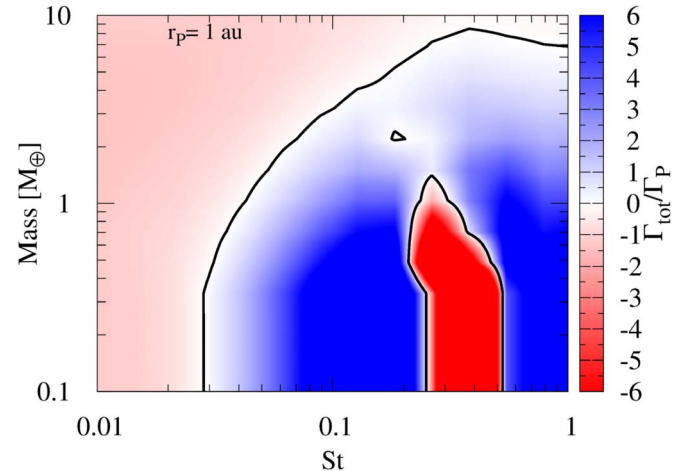


**Figure 5.** Same as Figure 2 but for the case of the nonisothermal disk.

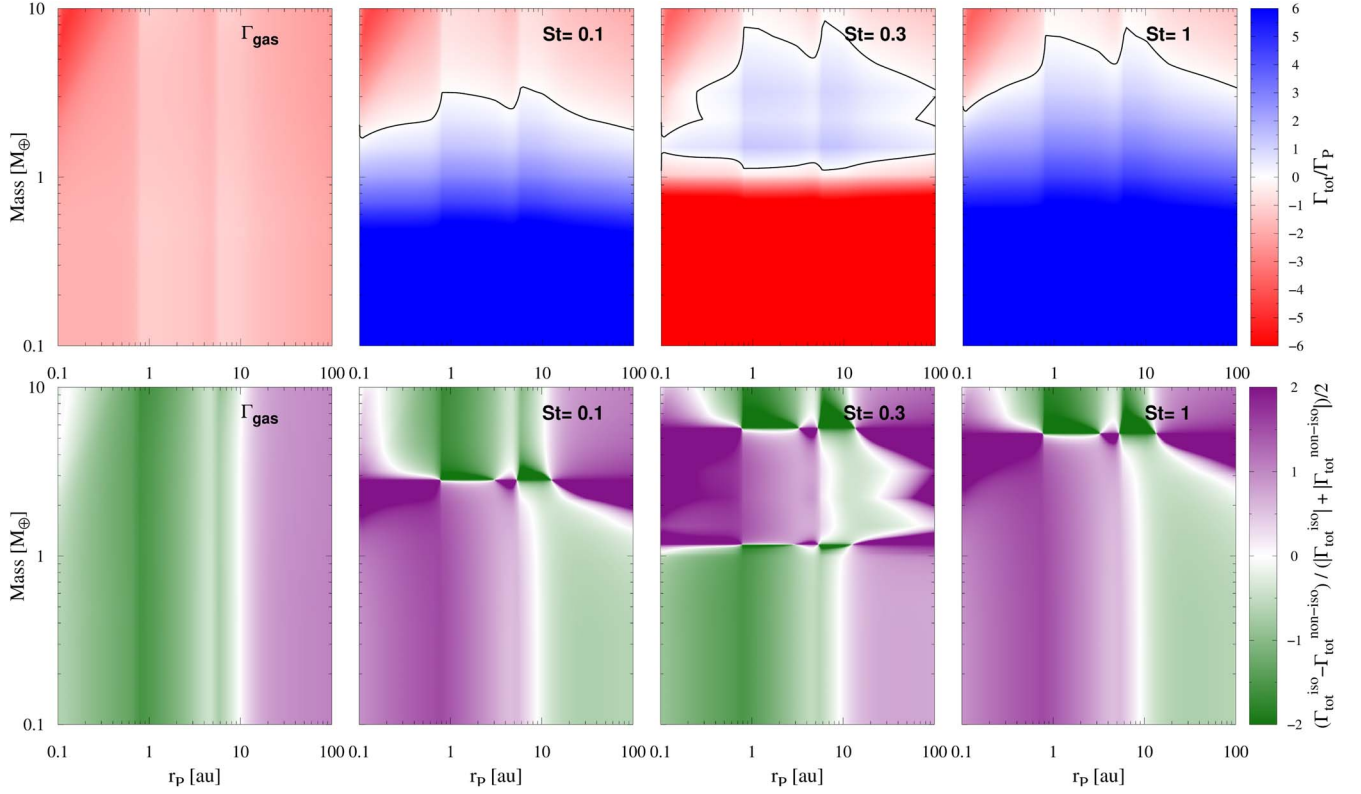


**Figure 6.** Top row: normalized torque maps,  $\Gamma_{\text{tot}}/\Gamma_p$ , as a function of planet mass and location for the nonisothermal disk model with  $\alpha = 3 \times 10^{-3}$ ,  $\dot{M}_* = 10^{-7} M_\odot \text{ yr}^{-1}$ , and dust-to-gas mass ratio  $\epsilon = 0.01$ . The disk model is described in detail in Section 4. Bottom row: normalized differential torque maps between the isothermal and nonisothermal cases.

#### 4.1. Dependence on Planet Location

The normalized torque map  $\Gamma_{\text{tot}}/\Gamma_p$  as a function of planet mass and location for the nonisothermal disk model with gas torque as provided in Jiménez & Masset (2017) is shown in the top row of Figure 6. The leftmost panel corresponds to a dust-free disk, whereas the subsequent panels show the results for dusty disks with three different (constant) Stokes numbers  $St = \{0.1, 0.3, 1\}$ . Similarly to the vertically isothermal disk, the total gas torque is always negative, implying inward planet migration. However, in this case, the gas torque presents a slightly more complex dependence on the location of the planet (see below).

The results for the dusty disks displayed in Figure 6 are qualitatively similar to the case of the isothermal disk; for the cases of  $St = 0.1$  and 1, the dust torque generates a significant region of positive total torque. In these two cases, different from the isothermal disk case, the value of the planet mass at which there is a transition between negative and positive torque regions depends on the planet’s location in the disk; see Figure 4. This nontrivial radial dependence, also observed to a lesser extent in the dust-free disk, is due to the fact that the radial structure for the nonisothermal disk deviates from power laws, and the Lindblad and corotation torques as provided in Jiménez & Masset (2017) depend on the disk diffusivity and viscosity.

For disks with dust particles with  $St = 0.3$ , the result is also qualitatively similar to the vertically isothermal disk. We find a total negative torque throughout the disk for low-mass (up to about  $\simeq 1 M_\oplus$ ) planets. As the mass of the planet increases (at a fixed location), the total torque becomes positive, but it

becomes negative again beyond a certain mass. As explained above, for nonisothermal disks, the mass threshold for the transition between regions of positive and negative total torque depends on the location of the planet due to the radial disk structure seen in Figure 4.

In order to illustrate the relative difference between the torque maps obtained for the isothermal and nonisothermal disk models considered, the bottom row of Figure 6 shows the associated differential torque map. The aim of this figure is to show how the radial dependence between both models differs, especially when the dust torque is included in the computation of the total torque. The radial structure of the normalized differential torque map in the dust-free case simply reflects the structure of the normalized nonisothermal gas torque map (the leftmost panel in the top row in Figure 6) because the normalized isothermal gas torque map is constant. When dust is present, the radial structure of the differential torque map is more complex. For  $St = 0.1$  and 1, there is a trend that, for low-mass planets wherein the total torque is positive, the total isothermal torque is larger (lower) than the total nonisothermal torque within (beyond)  $\sim 10$  au. For larger planets wherein the total torque is negative, the trend is the opposite; the total isothermal torque is lower (larger) than the total nonisothermal torque within (beyond)  $\sim 10$  au. For the case of  $St = 0.3$  and the regions where the total torque is negative, the total isothermal torque is more (less) negative than the nonisothermal within (beyond)  $\sim 10$  au. On the other hand, in the region where the total torque is positive, the total isothermal torque is lower (larger) than the nonisothermal within (beyond)  $\sim 10$  au.

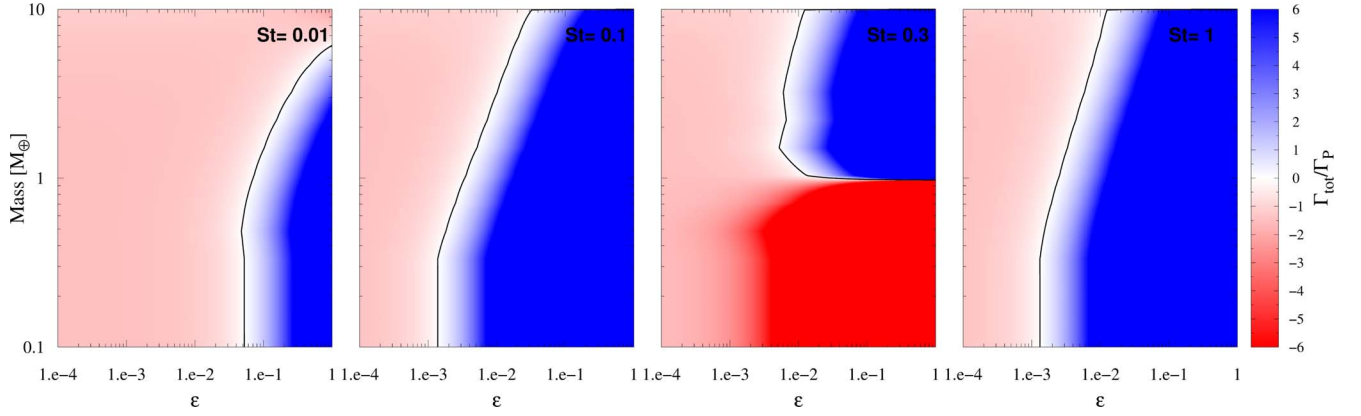


**Figure 7.** Normalized torque maps,  $\Gamma_{\text{tot}}/\Gamma_p$ , as a function of planet mass and dust-to-gas mass ratios computed at 1 au for a nonisothermal disk model with  $\alpha = 3 \times 10^{-3}$ ,  $\dot{M}_* = 10^{-7} M_\odot \text{ yr}^{-1}$ , and dust-to-gas mass ratio  $\epsilon = 0.01$ . The disk model is described in detail in Section 4. The panels correspond to different constant Stokes numbers  $St = \{0.01, 0.1, 0.3, 1\}$  from left to right.

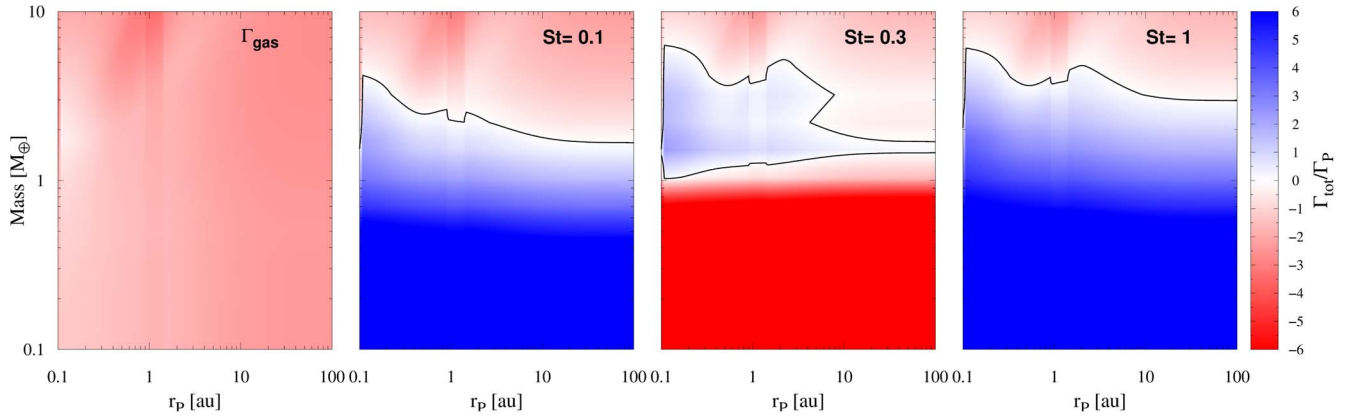


**Figure 8.** Same as Figure 6 but for a steady-state solution of a nonisothermal  $\alpha$ -disk using  $\dot{M}_* = 10^{-9} M_\odot \text{ yr}^{-1}$ .

#### 4.2. Dependence on Dust-to-gas Mass Ratio

The value of the dust-to-gas mass ratio can, in principle, depart significantly with respect to the fiducial value  $\epsilon = 0.01$ , and it is thus necessary to understand how the total torque on a planet changes accordingly. The normalized torque maps  $\Gamma_{\text{tot}}/\Gamma_p$  for the nonisothermal disk as a function of planet mass and dust-to-gas mass ratio,  $\epsilon$ , for four different Stokes numbers  $St = \{0.01, 0.1, 0.3, 1\}$  are shown in Figure 7. These torque maps correspond to a planet located at 1 au, but the results obtained at other locations in the disk are qualitatively similar.

As seen in Figure 7, planets with  $M_p \lesssim 0.5 M_\oplus$  embedded in a disk with dust with a small Stokes number,  $St \simeq 0.01$ , can be subject to strong positive torques for dust-to-gas mass ratios  $\epsilon \gtrsim 0.05$ . As the dust-to-gas mass ratio increases, the total torque becomes positive for planets with larger masses. Planets with masses in the range  $0.5\text{--}5 M_\oplus$  can still experience a positive net torque, provided the dust-to-gas mass ratio increases from  $\epsilon \simeq 0.05$  to 1. This dependence of the total torque on the dust-to-gas mass ratio may play an important role in the formation of planets by pebble accretion inside the water ice-line, where Stokes numbers tend to be small (O. M. Guilera et al. 2023, in preparation).

The morphology of the torque maps for  $St = 0.1$  and 1 is qualitatively similar to the case with  $St = 0.01$ . However, particles with these Stokes numbers, respectively associated with the gas- and gravity-dominated regimes discussed by BLP18, can exert large positive torques at significantly

lower dust-to-gas mass ratios. For instance, planets with  $M_p \lesssim 0.3 M_\oplus$  experience positive total torques for dust-to-gas mass ratios as low as  $\epsilon \gtrsim 2 \times 10^{-3}$ . Planets of higher masses require higher dust densities to experience positive total torques, but it is remarkable that planets as massive as  $10 M_\oplus$  experience positive torques for dust-to-gas mass ratios as low as  $\epsilon \gtrsim 2 \times 10^{-2}$ . This behavior may have important implications for the formation of planets by pebble accretion outside the water ice-line (see O. M. Guilera et al. 2023, in preparation).

For Stokes numbers in the transition region ( $St \simeq 0.3$ ), the torque map is very different, with positive total torques arising only when  $\epsilon \gtrsim 0.01$  and  $M_p \gtrsim 1 M_\oplus$  (at 1 au). Due to the strong dependence of the torques with the location of the planet in this regime (see Figure 6), we expect the range of masses and dust-to-gas mass ratios for outward migration to be sensitive to the planet’s distance to the central star.

#### 4.3. Dependence on Mass Accretion Rate

Protoplanetary disks typically evolve on timescales of the order of 1–10 Myr. During this evolution, the stellar mass accretion rate  $\dot{M}_*$  drops from about  $10^{-7} M_\odot \text{ yr}^{-1}$  for the youngest protostars to  $\simeq 10^{-9} M_\odot \text{ yr}^{-1}$  for the oldest ones. This reduction in the stellar mass accretion rate is associated with a lower disk gas surface density (Hartmann et al. 1998). This motivates the analysis of the dependence of the torque maps on the mass accretion rate  $\dot{M}_*$ .

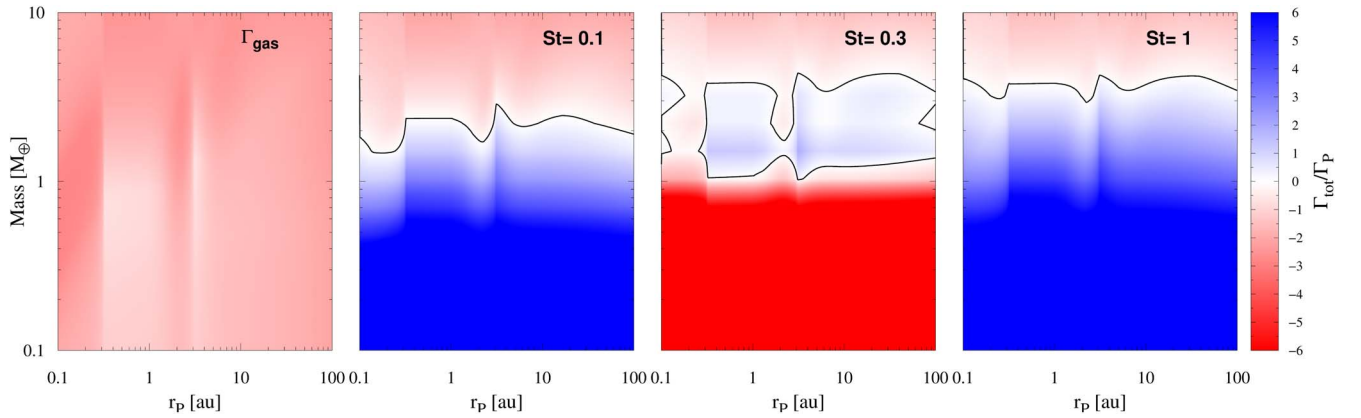


**Figure 9.** Same as Figure 6 but for a steady-state solution of the nonisothermal  $\alpha$ -disk using  $\alpha = 10^{-4}$ .

The normalized torque maps as a function of planet mass and location for a nonisothermal disk with  $\dot{M}_* = 10^{-9} M_\odot \text{ yr}^{-1}$  for a dust-free disk and a dusty disk with three different (constant) Stokes numbers  $St = \{0.1, 0.3, 1\}$  are shown in Figure 8. Note that even though the normalized torques are similar in magnitude to the case with  $\dot{M}_* = 10^{-7} M_\odot \text{ yr}^{-1}$ , the gas torque is about 1 order of magnitude lower for the lower accretion rate. This reflects the fact that the surface density of  $\alpha$ -disk models in a steady state decreases with decreasing mass accretion rate  $\dot{M}_*$  according to Equation (8).

The normalized torque map for the dust-free disk is very similar to the case with  $\dot{M}_* = 10^{-7} M_\odot \text{ yr}^{-1}$ , and the total torque is always negative. For disks with dust particles with Stokes number  $St = 0.1$ , the dust torque remains dominant, leading to a positive net torque, for planets with masses up to roughly  $\simeq 1.5$  and  $\simeq 4 M_\oplus$ . For Stokes number  $St = 1$ , the total torque remains positive for planets with higher masses, of the order of  $\simeq 3$ – $6 M_\oplus$ , depending on the planet location. We also note that in these last cases, despite the fact that they present similar trends to those observed for  $\dot{M}_* = 10^{-7} M_\odot \text{ yr}^{-1}$ , the radial dependence of the transition between positive and negative torques is different. In contrast to the behavior seen in Figure 6, for the higher accretion rate  $\dot{M}_* = 10^{-7} M_\odot \text{ yr}^{-1}$ , here the dust torque dominates closer to the central star. As the disk evolves and its accretion rate and surface density decrease, dust particles with either  $St = 0.1$  or 1 may be relevant for enabling low-mass planets in the inner disk regions to migrate outwards during the late stages of the disk evolution (see Section 6).

For  $St = 0.3$ , similar to the case with the accretion rate  $\dot{M}_* = 10^{-7} M_\odot \text{ yr}^{-1}$ , at a given disk location, there is a range of masses for which the total torque is negative. This mass range decreases from  $1 M_\oplus \lesssim M_p \lesssim 6 M_\oplus$  in the inner disk to  $2 M_\oplus \lesssim M_p \lesssim 3 M_\oplus$  in the outer disk. At lower accretion rates, the total torque is negative for almost all planet masses beyond  $r_p \gtrsim 7 \text{ au}$ .

#### 4.4. Dependence on the $\alpha$ -Viscosity Parameter

Here we analyze the dependence of the torque maps on the  $\alpha$ -viscosity parameter. We repeat the computations in Section 4 considering the values  $\alpha = 10^{-2}$  and  $10^{-4}$ . We note that in order to ease the comparison, we adopt different accretion rates than in the case of  $\alpha = 3 \times 10^{-3}$ . If we were to use the same value  $\dot{M}_* = 10^{-7} M_\odot \text{ yr}^{-1}$ , the disk gas surface density corresponding to  $\alpha = 10^{-4}$  would be much higher than for

$\alpha = 3 \times 10^{-3}$ . This is due to the fact that when the viscosity is decreased, the gas surface density needed to maintain a constant accretion rate throughout the disk must increase accordingly. The opposite occurs for  $\alpha = 10^{-2}$ . Thus, in order to achieve similar gas surface density profiles, we adopt  $\dot{M}_* = 3 \times 10^{-7} M_\odot \text{ yr}^{-1}$  for  $\alpha = 10^{-2}$  and  $\dot{M}_* = 3 \times 10^{-9} M_\odot \text{ yr}^{-1}$  for  $\alpha = 10^{-4}$ . We note that even though the gas surface density radial profiles are similar in these three cases, the corresponding midplane temperatures are higher for larger  $\alpha$  values, and the local midplane temperature gradients differ.

The normalized torque maps for  $\alpha = 10^{-4}$  and  $10^{-2}$  are shown in Figures 9 and 10, respectively. The trends observed are similar to the case with  $\alpha = 3 \times 10^{-3}$ . For the dust-free disk, the total torque is always negative. For  $St = 0.1$  and 1, the dust torque becomes the dominant contribution of the total torque, generating significant regions of positive torque. In the transition regime, for  $St = 0.3$ , we obtain negative total torques for the less massive and more massive planets and positive total torques for intermediate masses. The transition between regimes presents a complex radial dependence, and in the case of  $\alpha = 10^{-4}$ , the total torque is negative for all masses for planets located at  $r_p \simeq 0.2 \text{ au}$ .

It is worth noticing that the main features of the torque maps, including the magnitude of the normalized torques, are rather insensitive to the precise value of  $\alpha$ , a highly unknown parameter in real protoplanetary disks. For  $\alpha = 10^{-2}$ , dust diffusion may have a significant effect, particularly for particles with a small Stokes number. However, the contribution of such particles to the dust torque is less significant. Additional hydrodynamical calculations, including the effect of dust diffusion in highly turbulent disks, are required to characterize the dependence of dust torques on viscosity.

#### 4.5. Impact of Dust Size Distribution

In all previous sections, we have considered that the dust component can be characterized by a single Stokes number. Here we consider dust with a distribution of Stokes numbers. For illustrative purposes, and to ease the comparison with the results in the previous sections, we again adopt a steady-state, nonisothermal  $\alpha$ -disk with  $\alpha = 3 \times 10^{-3}$  and  $\dot{M}_* = 1 \times 10^{-7} M_\odot \text{ yr}^{-1}$  and a dust-to-gas mass ratio  $\epsilon = 0.01$ .

We briefly recall that for a mass distribution with  $dn/dm \propto m^{-\beta}$ , the total dust mass is  $\propto m^{2-\beta}$ . Thus, depending on whether  $\beta < 2$  or  $> 2$ , most of the mass of the system is

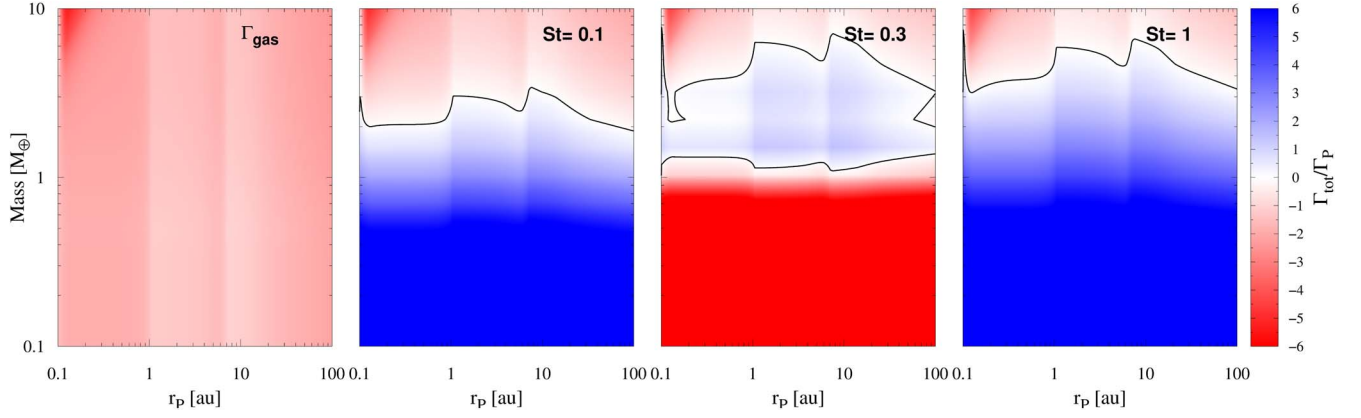


**Figure 10.** Same as Figure 6 but for a steady-state solution of the nonisothermal  $\alpha$ -disk using  $\alpha = 10^{-2}$ .

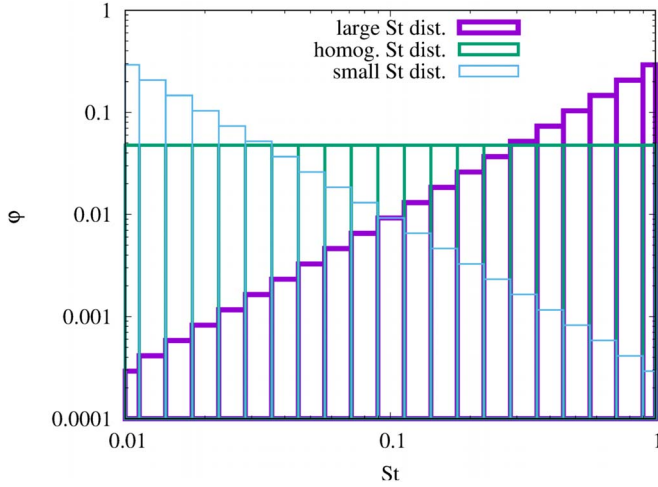


**Figure 11.** Histograms of the mass weights  $\varphi_i$  corresponding to the species  $i$  for each of the three mass distributions considered in Section 4.5.

contained in either the larger or the smaller particles, respectively. In addition, it is easy to show that the size distribution is given by  $dn/da \propto a^{3\beta-2}$ . In the Epstein drag regime, the Stokes number is proportional to the particle size, and thus  $dn/dSt \propto St^{3\beta-2}$ .

We consider three cases covering different characteristic possibilities: a distribution for which most of the mass is in small particles, with  $\beta = 5/2$  and  $dn/dSt \propto St^{-5.5}$ ; a homogeneous distribution, with  $\beta = 2$  and  $dn/dSt \propto St$ ; and a distribution for which most of the mass is in larger particles, with  $\beta = 3/2$  and  $dn/dSt \propto St^{-2.5}$ . For context, in the classical fragmentation equilibrium case,  $\beta = 11/6$ , and thus  $dn/dSt \propto dn/da \propto a^{-3.5}$  (Dohnanyi 1969), implying particle distributions for which most of the mass is in larger particles.

We represent the distribution of Stokes numbers with 21 evenly spaced bins in logarithmic scale between  $St = 0.01$  and 1. The dust species  $i$  contributes with a dust-to-gas mass ratio  $\epsilon_i = \varphi_i \epsilon$ , such that  $\sum_i \varphi_i = 1$  and thus  $\sum_i \epsilon_i = \epsilon$ . In Figure 11, we show the histograms of the mass weights for the three distributions considered. Note that in the case of  $dn/dm \propto m^{-5/2}$ , the four smallest Stokes numbers in the distribution contribute 75% of the mass, whereas for  $dn/dm \propto m^{-3/2}$ , the four largest Stokes numbers in the distribution contribute 75% of the mass. In the homogeneous distribution, each species has the same  $\varphi_i = 1/21$ .

The total dust torque can be computed as the sum of the dust torque exerted by each individual dust species,<sup>11</sup>

$$\Gamma_d = \sum_i \Gamma_d^i, \quad (13)$$

where  $\Gamma_d^i$  can be obtained from Equation (7) by setting  $\epsilon = \epsilon_i$  for each species.

The torque maps obtained for each distribution are shown in Figure 12. In the case where most of the mass is in the particles with lower Stokes numbers, the torque map is similar to the gas torque (left panel of Figure 6), and the solids do not play a significant role. On the other hand, for the homogeneous distribution and the distribution where most of the mass is contained in large Stokes number particles (middle and bottom panels in Figure 12), the dust torque dominates and generates regions of positive torque for planets with masses up to  $\simeq 3$  and  $\simeq 7 M_\oplus$ , respectively. These results suggest that dust growth models in which most of the mass remains in the form of large particles (e.g., Birnstiel et al. 2012) favor outward migration of low-mass planets provided these particles have  $St \simeq 0.1$ –1. As we show in O. M. Guilera et al. (2023, in preparation), these results may have important implications for the role of the dust torque on the migration of low-mass planets growing by pebble accretion.

## 5. Planet Migration

Using the models for the gas and dust torques as described in Section 2.1, we can integrate the equations of motion for an embedded planet to obtain its migration history in the disk. In order to accomplish this, we implement a simple model in which the planet mass grows by accretion of pebbles with a fixed Stokes number. For simplicity and consistency, we evolve only one planet at a time. We consider initial conditions at  $r_p = \{1, 5, 10\}$  au, and the initial mass of the planet is  $0.1 M_\oplus$  in all cases. The orbital integration is terminated when either of the following conditions is met: the planet grows to  $10 M_\oplus$  or reaches the inner/outer disk edge located at 0.1/100 au. We note here that in general, these conditions are fulfilled in less than  $\sim 1$  Myr for the cases of moderate and high pebble accretion rates ( $10^{-5}$  and  $10^{-4} M_\oplus \text{ yr}^{-1}$ , respectively) and less than 5 Myr for the case of a low pebble accretion rate ( $10^{-6} M_\oplus \text{ yr}^{-1}$ ).

<sup>11</sup> This is valid provided the dust does not transfer momentum to the gas and all dust species interact only via the gas.

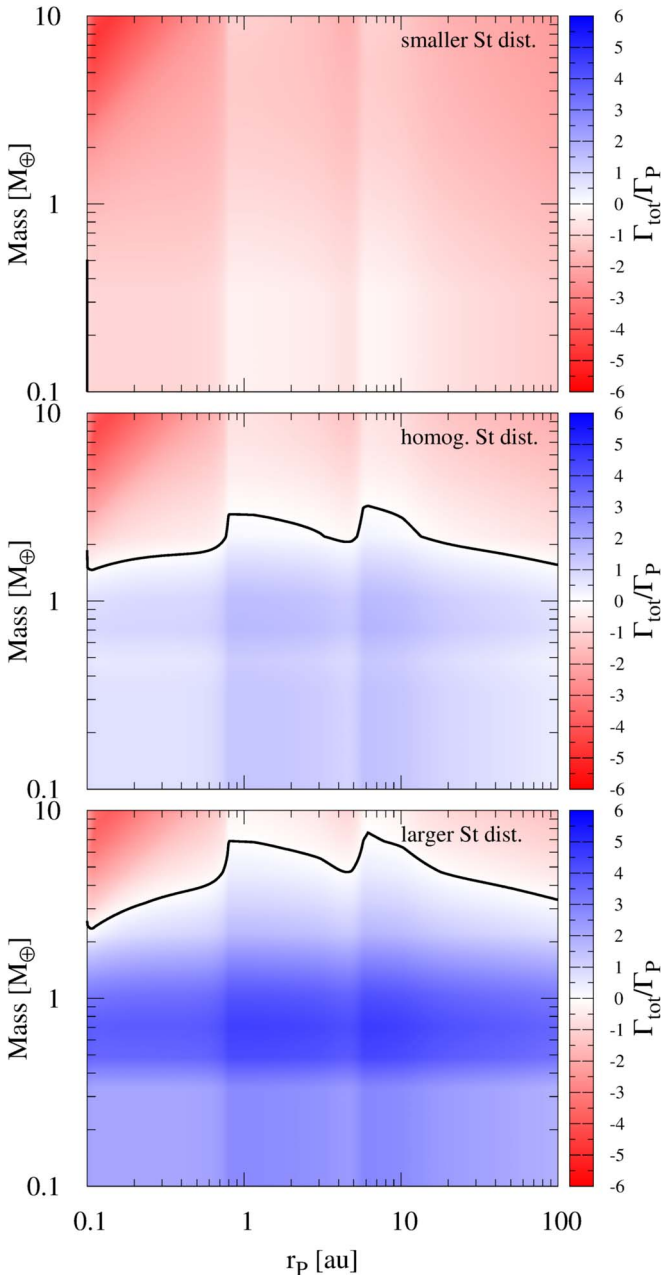


**Figure 12.** Same as Figure 6 but considering a Stokes number distribution between  $St = 0.01$  and 1. The top panel shows the case where particles with the smaller size/Stokes number contribute the most to the mass of solids in the disk. The middle panel represents the case of a homogeneous mass (or Stokes number) distribution, while the bottom panel corresponds to the case where the mass of solids in the disk is dominated by the larger particle size/Stokes numbers.

### 5.1. Steady-state Isothermal Disk Models

We first consider a steady-state, vertically isothermal  $\alpha$ -disk model with  $\alpha = 3 \times 10^{-3}$  and constant stellar accretion rate  $\dot{M}_* = 10^{-7} M_\odot \text{ yr}^{-1}$ . When dust is present, the dust-to-gas mass ratio is  $\epsilon = 0.01$ , and the Stokes number takes a fixed value with  $St = \{0.1, 0.3, 1\}$ . We consider three constant values for the accretion rate of solids onto the planet according to  $\dot{M}_p = \{10^{-4}, 10^{-5}, 10^{-6}\} M_\oplus \text{ yr}^{-1}$ . The resulting formation tracks in dusty disks are shown in the left column of Figure 13 with solid lines. For reference, the formation tracks in the dust-free disks, exhibiting inward migration, are

shown with dashed lines. We remark here that, under our steady-state assumption, the high mass accretion rate assumed implies that the disk gas surface density remains high during the planet’s formation and migration. In this regard, this choice provides a reference case for the early stages of a more realistic disk evolution model. We note that, in a steady state, the associated integrated disk mass between 0.1 and 40 au is about  $0.1 M_\odot$ , which corresponds to a gravitational stable disk under the classical Toomre stability criterion. The total gaseous disk mass between 0.1 and 100 au is  $\sim 0.3 M_\odot$ , which is too massive for typical protoplanetary disks. However, when we consider disk models that evolve in time below (Section 5.3), we implicitly assume that the disk is initially massive and compact and that, as the mass accretion rate decreases, the disk mass decreases and spreads viscously.

As seen in Figure 13, planets initially migrate outwards for  $St = 0.1$  and 1. In the case of  $St = 0.1$ , the outward migration continues until they reach  $\approx 3 M_\oplus$  (for  $\dot{M}_p = 10^{-4}$  and  $10^{-5} M_\oplus \text{ yr}^{-1}$ ) or 100 au (for  $\dot{M}_p = 10^{-6} M_\oplus \text{ yr}^{-1}$ ). Similar behavior occurs for  $St = 1$ , where planets migrate outwards until they reach  $\approx 5.5 M_\oplus$  for  $\dot{M}_p = 10^{-4} M_\oplus \text{ yr}^{-1}$ , while for  $\dot{M}_p = 10^{-5}$  and  $10^{-6} M_\oplus \text{ yr}^{-1}$ , they continue migrating outwards until they reach 100 au.

For  $St = 0.3$ , planets migrate inwards at early times in all cases, in agreement with the torque map shown in Figure 3. For the case of a solid accretion rate of  $\dot{M}_p = 10^{-6} M_\oplus \text{ yr}^{-1}$ , planets do not reach the needed mass ( $\approx 1 M_\oplus$ ) to reverse the inward migration, and they reach the inner disk at 0.1 au very fast with masses under  $0.5 M_\oplus$ . For  $\dot{M}_p = 10^{-5} M_\oplus \text{ yr}^{-1}$ , planets reverse the inward migration and migrate outwards until they reach  $\approx 6 M_\oplus$ . After reaching this mass, their migration reverses again so that they migrate fast inwards, reaching  $10 M_\oplus$  at the inner disk edge. For the highest solid accretion rate we consider,  $\dot{M}_p = 10^{-4} M_\oplus \text{ yr}^{-1}$ , the planets grow fast enough that they do not migrate significantly before they reach  $10 M_\oplus$ .

Whether or not dust is present has a more significant impact on the formation tracks when the solid accretion rate is lower. Naturally, planets that reach  $M_p \approx 10 M_\oplus$  fast enough do not have the chance to spend significant time in the region of the torque maps where the dust contribution is important. The situation is different when the accretion of solids is slower. In particular, for  $\dot{M}_p = 10^{-5}$  or  $10^{-6} M_\oplus \text{ yr}^{-1}$  and dust with  $St = 0.1$  and 1, planets can remain in disk regions where they are subject to positive torques for longer times, significantly affecting their formation tracks with respect to the dust-free case.

### 5.2. Steady-state Nonisothermal Disk Models

We now consider a steady-state, nonisothermal  $\alpha$ -disk model with  $\alpha = 3 \times 10^{-3}$  and constant stellar accretion rate  $\dot{M}_* = 10^{-7} M_\odot \text{ yr}^{-1}$  and evolve an embedded planet sweeping the same set of initial conditions and physical parameters we used for the vertically isothermal disk. The formation tracks in steady-state, nonisothermal dusty disks are shown in the middle column of Figure 13 with solid lines. For reference, the formation tracks in the dust-free disks, exhibiting inward migration, are also shown with dashed lines.

Overall, the planet formation tracks for nonisothermal disks are qualitatively similar to the ones computed for vertically isothermal disks. Some of the results worth highlighting are as follows. (i) In dusty nonisothermal disks, in contrast to the

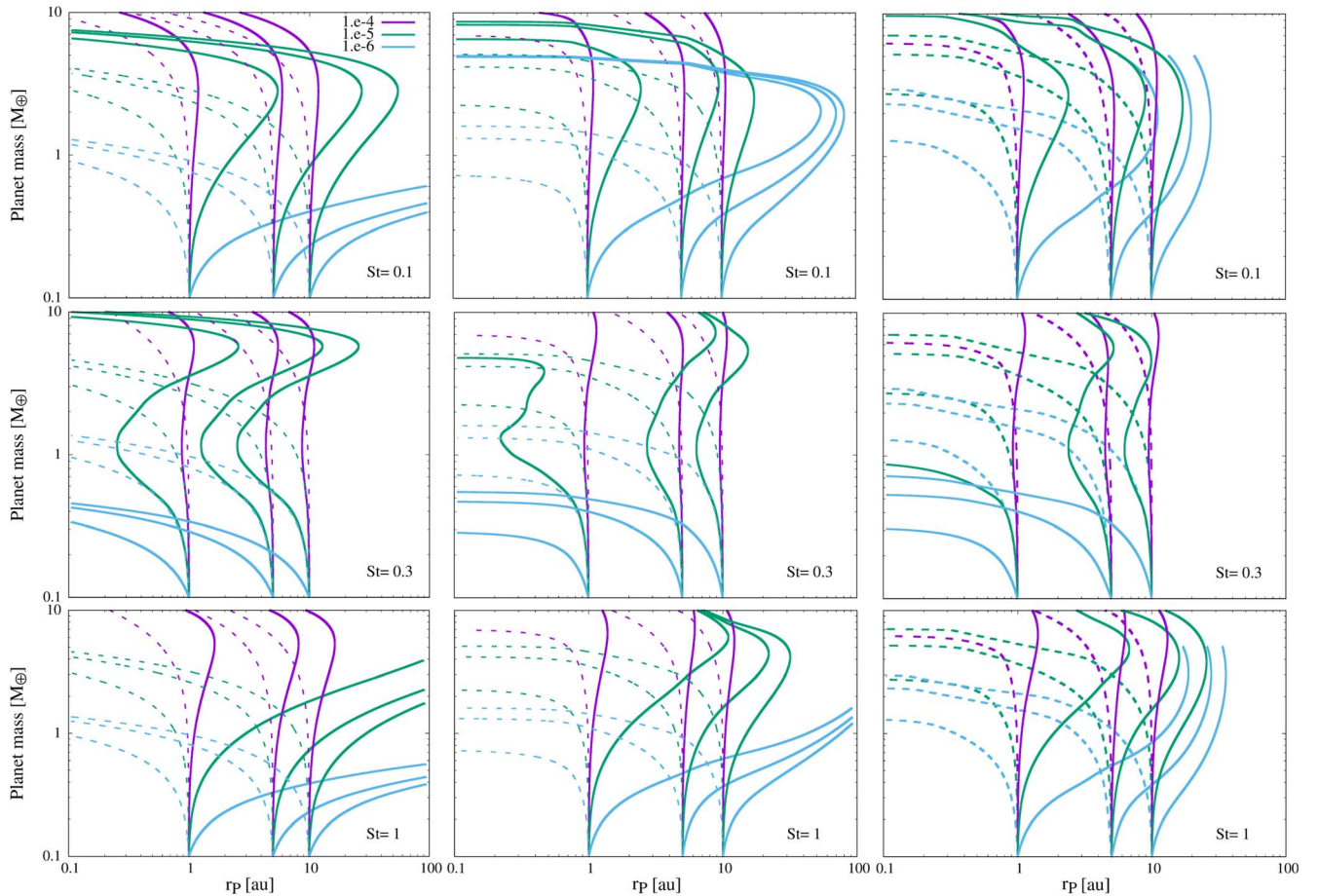


**Figure 13.** Formation tracks for planets initially located at  $r_p = \{1, 5, 10\}$  au evolving in different disk models. The results corresponding to steady-state isothermal disks (see Section 3), steady-state nonisothermal disks (see Section 4), and time-dependent nonisothermal disks (see Section 5.3) are shown in the left, middle, and right columns. Each row of panels shows a given Stokes number in  $St = \{0.1, 0.3, 1\}$ . Solid lines represent tracks of planets in dusty disks with a constant dust-to-gas mass ratio  $\epsilon = 0.01$  growing via pebble accretion with  $\dot{M}_p = \{10^{-4}, 10^{-5}, 10^{-6}\} M_\oplus \text{ yr}^{-1}$  (violet, green, and cyan lines, respectively). Dashed lines show the corresponding formation tracks in dust-free disks.

isothermal case, the transition from outward to inward (or inward to outward) planet migration does not occur at the same planet mass, in agreement with Figure 6. (ii) In dusty nonisothermal disks with  $St = 0.1$ , none of the planets reach 100 au when the solid accretion rate is  $\dot{M}_p = 10^{-6} M_\oplus \text{ yr}^{-1}$ . These planets reach  $\simeq 2 M_\oplus$  and reverse their initial outward migration somewhere between  $\sim 50$  and  $\sim 80$  au, depending on their initial locations. They all reach the inner disk edge with roughly the same mass,  $\sim 5 M_\oplus$ . A similar behavior is observed for the case of  $St = 1$  and  $\dot{M}_p = 10^{-5} M_\oplus \text{ yr}^{-1}$ . (iii) Similar to the isothermal disk cases, for high rates of accretion of solids, e.g.,  $\dot{M}_p = 10^{-4} M_\oplus \text{ yr}^{-1}$ , the planet formation tracks are rather insensitive to the presence of dust. This is especially true for the planets initially located at 5 and 10 au due to fast planet formation timescales.

### 5.3. Evolving Nonisothermal Disk Models

We consider here a simple model for the temporal evolution of a nonisothermal disk as the stellar accretion rate decreases in time. We adopt the same model considered in Bitsch et al. (2015), in which the disk evolves through a succession of steady-state solutions wherein the mass accretion rate  $\dot{M}_\star$

decreases in time according to

$$\log\left(\frac{\dot{M}_\star}{M_\odot \text{ yr}}\right) = -8 - 1.4 \times \log\left(\frac{t + 10^5 \text{ yr}}{10^6 \text{ yr}}\right). \quad (14)$$

This parameterizes a smooth transition between a mass accretion rate of  $10^{-7}$  and  $10^{-9} M_\odot \text{ yr}^{-1}$  in 5 Myr. As time advances and the mass accretion rate decreases, the gas surface density decreases accordingly. As in the steady-state disk models considered above, we set  $\alpha = 3 \times 10^{-3}$ . We compute a dense grid of 50 steady-state  $\alpha$ -disk models with equally spaced accretion rates  $\dot{M}_\star$  between the initial and final accretion rates. We interpolate between these 50 models as needed to obtain a smooth disk evolution in time. For simplicity, we assume that the dust-to-gas mass ratio  $\epsilon$  remains constant as the disk density evolves in time. This provides a conservative approach to assess the impact of dust in altering the planetary formation tracks with respect to the dust-free disks.

In the background of these time-dependent, nonisothermal disk models, we evolve an embedded planet sweeping the same set of initial conditions and physical parameters we used for the steady-state disk models. The resulting formation tracks in dusty disks are shown in the right column of Figure 13 with solid lines. For reference, the formation tracks in the dust-free

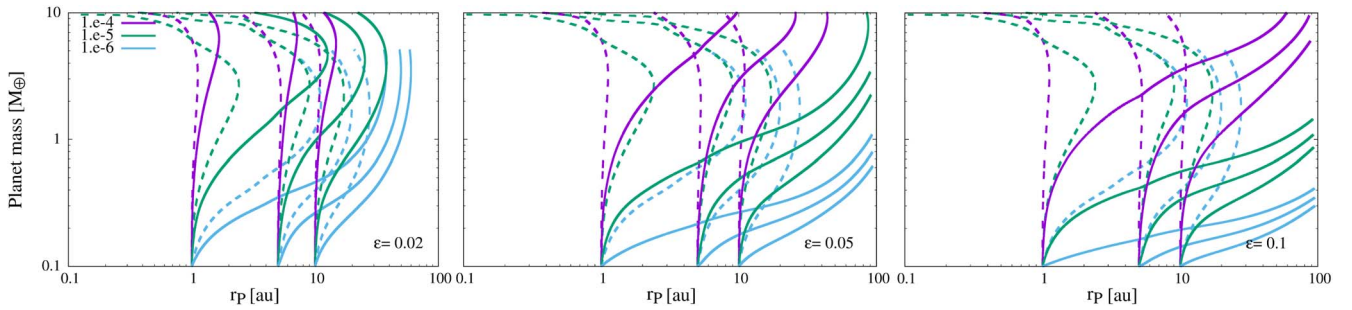


**Figure 14.** Formation tracks for planets initially located at  $r_p = \{1, 5, 10\}$  au evolving in a time-dependent nonisothermal disk (see Section 5.3) with a solid component with Stokes number  $St = 0.1$ . The results corresponding to different gas-to-dust mass ratios in  $\epsilon = \{0.02, 0.05, 0.1\}$  are shown in the left, middle, and right columns, respectively. Solid lines represent tracks of planets growing via pebble accretion with  $\dot{M}_p = \{10^{-4}, 10^{-5}, 10^{-6}\} M_\oplus \text{ yr}^{-1}$  (violet, green, and cyan lines, respectively). Dashed lines show the corresponding formation tracks in disks with  $\epsilon = 0.01$ .

disks exhibiting inward migration are shown with dashed lines. Note that for the highest pebble accretion rate considered,  $\dot{M}_p = 10^{-4} M_\oplus \text{ yr}^{-1}$ , the formation tracks are similar to the ones in steady-state disks, irrespective of the Stokes number. This is due to the fact that formation timescales are shorter than migration timescales, and planets form fast enough that the disk evolution does not affect the planet formation process.

For the cases with pebble accretion rates  $\dot{M}_p = 10^{-5} M_\oplus \text{ yr}^{-1}$ , the planet formation tracks present some differences with respect to the steady-state, nonisothermal dust-free disk. However, these are not as noticeable as those for the solid accretion rate  $\dot{M}_p = 10^{-6} M_\oplus \text{ yr}^{-1}$ . This is particularly the case for Stokes numbers  $St = 0.1$  and 1, for which planets in steady-state disks end at 0.1 au with  $5 M_\oplus$  and 100 au with  $2 M_\oplus$ , respectively. In contrast, in evolving disks, all of the planets reach  $5 M_\oplus$  in 5 Myr in moderate to extended orbits, i.e., between  $\simeq 5$  and  $\simeq 30$  au, depending on their initial locations. As the gas torque on the planet decreases, due to the decreasing gas surface density of the disk, the planets are allowed to remain in orbits with moderate to extended radii for longer times. Clearly, disk evolution plays an increasingly significant role the slower the planets grow.

#### 5.4. Impact of the Dust-to-gas Mass Ratio

As stated in Section 2, in the absence of dust feedback on the gas, the dust torque scales linearly with the dust-to-gas mass ratio. In order to explore the impact of the dust-to-gas mass ratio on the planet formation tracks, we consider the set of values  $\epsilon = \{0.02, 0.05, 0.1\}$ . If protoplanetary disks have dust-to-gas mass ratios similar to the metallicity of their host protostars, values of up to  $\epsilon = 0.03$  could be found in disks around metal-rich stars. Higher values of dust-to-gas mass ratios, in at least some disk regions, could be achieved via other mechanisms. For instance, the dust-to-gas mass ratio can increase in the inner disk regions due to dust drifting from larger radii (e.g., Drazkowska et al. 2016). Dust-to-gas mass ratios near unity have been envisioned to be reached in preferential locations in protoplanetary disks (e.g., Drazkowska & Alibert 2017). As an example, we consider a fixed dust-to-gas mass ratio throughout the disk and compute the planet formation tracks for  $St = 0.1$  assuming that the gaseous disk evolves in time according to Equation (14).

The impact of the dust-to-gas mass ratio on a sample of evolutionary tracks is shown in Figure 14. It is seen that for dust-to-gas mass ratios with  $\epsilon \gtrsim 0.05$ , planets can migrate

significantly outwards, even for the highest solid accretion rate we considered,  $\dot{M}_p = 10^{-4} M_\oplus \text{ yr}^{-1}$ . For the models with lower solid accretion rates, the effect of larger dust-to-gas mass ratios is increasingly dominant for outward planet migration, irrespective of Stokes number. As we will show in a follow-up paper (O. M. Guilera et al. 2023, in preparation), enhanced dust-to-gas mass ratios in the inner disk regions, e.g., due to dust drifting from outer disk regions, can have a significant impact on the migration of growing planetary cores inside the water ice-line.

## 6. Summary and Discussion

While planet migration has been extensively studied in gaseous disks, the effect of solids on this process has not yet been addressed. Measurements of dust torques have been reported by BLP18, but the effect of these torques on the migration of planetary embryos has remained an open question. Aiming at filling this gap, in this work we quantify for the very first time the impact of the torque arising from solids on planet migration and assess its role in the formation tracks of planetary embryos embedded in classical protoplanetary disk models.

Based on the torque measurements of BLP18, we computed what we refer to as “torque maps” in order to quantify the importance of the dust torque (with respect to the gas torque) in terms of the disk thermodynamics, planet location, stellar mass accretion rate, dust-to-gas mass ratio, level of turbulent viscosity, and different dust size distributions. Subsequently, we investigated how the migration of growing planets is affected by disk thermodynamics, dust content, and global evolution.

In order to make progress in an inherently complex problem, we have made a number of simplifying assumptions and approximations. This approach enabled us to obtain the first quantitative estimates for the impact of the dust torque under a very wide range of physical conditions. Some of the effects we have found could become more or less prominent when models alleviating the caveats mentioned below are considered. Because of this, the theoretical formation path that a planetary core follows may depend on the details of the models employed. Nevertheless, it is worth stating some of the consequences associated with the broad trends that emerge from the results we obtained using standard assumptions to model the disk and its solid content.

### 6.1. Implications

Our findings have a series of implications for the processes involved in the formation and evolution of planetary cores in dusty disks. These, in turn, determine not only the formation timescales, final masses, and location of the planetary embryos but, potentially, also the final compositions of the resulting planets.

#### 6.1.1. Low-mass Planets Migrate Outwards beyond the Water Ice-line

Dust growth models suggest that most of the mass in solids is contained in particles at the high end of the particle size distribution (e.g., Birnstiel et al. 2012; Stammer & Birnstiel 2022). In addition, Venturini et al. (2020a) and Drazkowska et al. (2021) showed that the mass-averaged Stokes number of the dust distribution is  $St \sim 0.1$  beyond the water ice-line (see their Figures 1 and 4, respectively). Thus, the results presented in Section 4.5 imply that forming planets of up to a few Earth masses located beyond the water ice-line migrate outwards, unless the dust-to-gas mass ratio becomes lower than  $\sim 10^{-3}$  (see Section 4.2).

#### 6.1.2. Small Stokes Numbers Could Matter in Dust-rich Disks

Under a number of circumstances, the dust-to-gas mass ratio could increase significantly in some disk regions. This could occur in the inner part of the disk due to radial pebble drift from the outer disk (e.g., Drazkowska et al. 2016; Venturini et al. 2020b), near the water ice-line due to water vapor recondensation (e.g., Drazkowska & Alibert 2017; Schneider & Bitsch 2021), or in a pressure bump where pebbles could accumulate (e.g., Pinilla et al. 2012; Zhu et al. 2012; Weber et al. 2018; Guilera et al. 2020; Morbidelli 2020; Chambers 2021; Jiang & Ormel 2023). This implies that if the dust-to-gas mass ratio reaches, for example,  $\epsilon = 0.1$ , even particles with Stokes numbers as small as  $St = 0.01$  can exert significant torques if most of the mass is in those particles (Figure 7).

#### 6.1.3. Forming Planets in Extended Orbits in Dust-rich Disks

Disks with a large content of solids favor outward migration. This may offer a mechanism for the cores that start their formation in the inner disk region to end up located far from the central star, at tens of au (see Figures 13 and 14). Moreover, these planets that migrate outwards, up to tens of au, could act as seeds for the formation of more massive planets in wide orbits. This could offer a natural path to explain the formation of these controversial objects, which are usually invoked as responsible for the ring and gap structures observed in protoplanetary disks by the Atacama Large Millimeter/submillimeter Array (ALMA; e.g., Andrews 2020).

### 6.2. Current Caveats and Future Lines of Work

Here we state and assess our most important hypothesis and mention future lines of work aimed at building more realistic models. More accurate and consistent models for the gas (and dust) torque could be obtained with dedicated, systematic numerical simulations considering more detailed disk models.

#### 6.2.1. Precomputed Prescriptions for Type I Migration

Even though the disk models we consider have a nontrivial radial and thermodynamic structure, we adopted the torque

prescriptions of Tanaka et al. (2002), derived for globally isothermal disks with power-law radial structure, and Jiménez & Masset (2017), derived for adiabatic disks. These prescriptions for the gas torque neglect migration feedback (see, e.g., Paardekooper 2014), an effect that is more pronounced in low-viscosity disks (see the review of Paardekooper et al. 2022).

#### 6.2.2. Caveats Inherited from BLP18

By construction, our results contain all of the caveats involved in computing the dust torques in BLP18. In particular, the numerical simulations involved are 2D and thus insensitive to the vertical disk structure. More realistically, in three dimensions, the results are expected to depend on the vertical distribution of the solid component, which is sensitive to the level of vertical diffusion of solids, as regulated by the level of turbulence in the disk. Additional studies of dust torques properly considering the turbulent diffusion of solids are needed to better quantify the magnitude of dust torques. Moreover, simulations in BLP18 only considered disks with radial  $(-1/2)$  power-law gas surface density structures. How the magnitude of dust torques is affected by the underlying gas disk model is still uncertain and could potentially affect some detailed aspects of our results. In particular, we assumed that the dust torque does not depend on the gas torque (but see Appendix), which implicitly assumes that the underlying gas disk model is not significantly important. This, however, may not necessarily be the case for solids that are highly coupled to the gas. Also, in BLP18, it is assumed that solids behave as a pressureless fluid, which is reasonable for solids that are very well coupled to the gas. However, when solids are barely coupled, this approximation could break down. Furthermore, the dust torque measurements of BLP18 do not include the effect of planetary motion. Migration modifies the relative drift between solids and the planet and is expected to modify the shape and magnitude of the dust distribution asymmetry developed close to the planet, which could either enhance or diminish the dust torques. Moreover, if the planet migrates, it may develop eccentricity. Additional hydrodynamical simulations are needed in order to quantify the impact of eccentricity on dust torques. It is also worth recalling that the effective smoothing length used in the 2D simulations in BLP18 can affect the measured values of the dust torques, as confirmed by Regály (2020). The dust torque in the gravity-dominated regime is robust because it arises from a large-scale asymmetry. However, in the gas-dominated regime, the dust torque occurs due to a subtle asymmetry in the dust density distribution close to the planet (BLP18). In order to minimize spurious measurements due to unresolved dynamics, BLP18 conservatively cut off the inner half of the Hill sphere to compute the torques. Nevertheless, 3D simulations, where the smoothing length is not a free parameter, are needed to more accurately quantify the dust torque in different regimes. Thermodynamic effects could be important for dust torques. For example, the equation of state used could affect the gas dynamics and may have a nonnegligible effect on the solid dynamics (see, e.g., Miranda & Rafikov 2019). Also, the effect of pebble accretion can change the dust asymmetry around the planet, and hence the magnitude of the dust torque (see, e.g., Regály 2020), and generate heat that would lead to heating torques (e.g., Benítez-Llambay et al. 2015; Masset 2017), an effect that, for simplicity, we do not consider in this first work. Finally, the dust back-reaction force (feedback) is neglected in BLP18. This

implicitly assumes that the density contrast of the solids remains low throughout the disk and close to the planet. However, a large density contrast of solids is observed in the numerical simulations in [BLP18](#), which may have an impact on the dynamics of gas and solids close to the planet. Further work including the dust feedback is needed to assess the impact of this approximation.

### 6.2.3. Extrapolating [BLP18](#)'s Results to Different Disk Models

In order to extrapolate the results of [BLP18](#) to other disk models, we assumed a particular scaling of the dust torque with the disk parameters; see Equation (7). However, the dust torque could scale also with other physical disk parameters that we do not consider here. In order to assess the robustness of our results, in [Appendix](#), we assume an alternative model where the dust torque is proportional to the gas torque (see Equation (16)) and compare the results. We show that our main results and conclusions are insensitive to the specific choice.

### 6.2.4. Pebble Accretion, Stokes Number/Dust Size Distributions

In order to compute the migration of the growing planetary embryos, we adopted constant pebble accretion rates and Stokes numbers (see Section 5). A number of models usually adopt solid particles with a constant Stokes number or size throughout the disk with pebble fluxes that decay in time, decreasing the pebble accretion rate on the planet (e.g., [Lambrechts et al. 2019](#); [Ogihara & Hori 2020](#)). In more realistic planet formation models that include dust growth and evolution, both the pebble Stokes numbers and the pebble flux evolve in time, and throughout the disk, in a more complex way (e.g., [Venturini et al. 2020a](#); [Draskowska et al. 2021](#)).

### 6.2.5. Isolated Planets

Our study assumes that a planet evolves in the disk in isolation. In order to extrapolate our results to disks containing multiple planets, it would need to be assumed that migrating planets can be modeled independently of each other. This assumption will not hold in compact systems where the gravitational interaction between cores and planets could be significant. Also, multiple migrating cores are expected to exert strong perturbations on the dust surface density that can propagate from the outermost planet inward via radial drift (see, e.g., Figure 4 in [BLP18](#)). The conditions for significant interference between multiple planets could, in principle, be assessed with targeted numerical simulations. In addition, when multiple planets grow simultaneously, if one of them becomes massive enough to open a gap or partial gap on the disk, the flux of pebbles to the planets in the inner orbits can be halted (e.g., [Lambrechts et al. 2014](#); [Weber et al. 2018](#)). This situation could also affect the magnitude of the dust torque for the inner planets.

### 6.2.6. Disk Gaps Induced by Photoevaporation

For simplicity, the classical disk models we adopted neglected the effects of photoevaporation due to the central star. In low-mass stars, X-rays are the dominant source of photoevaporation (see, e.g., [Kunitomo et al. 2021](#)). [Venturini et al. \(2020b\)](#) showed that X-ray photoevaporation can open a gap in the gas disk at a few au on a typical timescale of 1–2 Myr. This gap prevents the pebble flux from reaching the

inner disk, significantly affecting pebble accretion onto the planets there. Thus, more realistic gas disk evolution models should also affect the computation of the dust torque. In a follow-up paper ([O. M. Guilera et al. 2023](#), in preparation), we will incorporate the computation of the dust torque in PLANETALP, our global framework for modeling planet formation, in order to study its effects on planet migration in more realistic settings for modeling planet formation.

### 6.2.7. Disk Viscosity

Our work is based on the assumption that the disk remains laminar so we can describe the gaseous torques by simple prescriptions. Also, we used measurements of dust torques in [BLP18](#) in laminar viscous disks. However, planets embedded in low-viscosity disks can induce vortices, which affect not only the gas (see, e.g., [Paardekooper 2014](#); [McNally et al. 2019](#); [Hsieh & Lin 2020](#)) but also the dust torque. Thus, caution is needed when extrapolating our results to low-viscosity or wind-driven disks.

## 7. Takeaways and Conclusion

Here we summarize the most relevant takeaways from our study, emphasizing the results that we expect not to depend too sensitively on our main assumptions and approximations.

### 7.1. Main Takeaways

1. The dust torque can contribute significantly to the total torque acting on a planetary embryo,  $M_p \lesssim 10 M_\oplus$ , for standard values of the dust-to-gas mass ratio, i.e.,  $\epsilon = 0.01$  (see Figures 2, 5, and 6).
2. The dust torque is positive in the vast majority of the parameter space spanned by  $0.1 \leq M_p/M_\oplus \leq 10$  and  $0.01 \leq St \leq 1$  for  $\epsilon = 0.01$ . The relative magnitude between the gas and dust torque components depends on the Stokes numbers of dust particles.
3. There are two regimes where the dust torque dominates significantly for  $M_p \lesssim 10 M_\oplus$ : gas-dominated,  $St \simeq 0.1$ , and gravity-dominated,  $St \gtrsim 0.5$ . These regions are associated locally with outward migration. This outcome is robust for a wide range of disk parameters, such as the stellar mass accretion rate,  $\alpha$ -viscosity parameter, and/or disk thermodynamics adopted.
4. In the transition region between the previous two, i.e.,  $St \simeq 0.2\text{--}0.5$  and  $M_p/M_\oplus \leq 10$ , the value of the dust torque is sensitive to all of the parameters involved (e.g., viscosity, stellar accretion rate, and planet location), and the direction of migration depends on the details.
5. If there are disk regions with enhanced dust-to-gas mass ratios of order  $\epsilon = 0.1$ , even particles with Stokes numbers as low as  $St \lesssim 0.01$  can exert a significant torque (see Figure 7). At these higher dust concentrations, the torque exerted by larger dust particles can influence the dynamics of planets with masses larger than  $M_p \simeq 10 M_\oplus$ .
6. The results outlined above do not depend sensitively on the stellar mass accretion rate or the  $\alpha$ -viscosity parameter (Sections 4.3 and 4.4, respectively) or whether the dust particles are assumed to have a unique Stokes number or are distributed in a range.
7. The properties of the torques as described above dictate the local dynamics of a planetary embryo in a dusty disk.

Given that the relative magnitude of the gas and dust torque components evolves as the embryo migrates and grows, its long-term dynamics depends on the accretion rate onto the planet, the global disk structure, and/or its long-term evolution.

8. Even though the details of the evolutionary tracks are sensitive to various physical parameters, we find that under the set of assumptions usually invoked, dust torques can have a significant impact during significant fractions of the formation history of planetary embryos by halting or reversing inward migration. The impact of the dust component naturally decreases for planetary embryos that grow too fast, e.g.,  $\dot{M}_p \simeq 10^{-4} M_{\oplus} \text{ yr}^{-1}$ , or disks that run out of material too quickly (see Figure 13).

The most important implications of our findings can be summarized as follows. (i) Low-mass planets migrate outwards beyond the water ice-line if most of the mass in the solids is in larger particles there. (ii) The torque due to solids with small Stokes numbers,  $St \simeq 0.01$ , can play a dominant role in disks with a moderately high dust-to-gas mass ratio,  $\epsilon \simeq 0.02\text{--}0.05$ , if most of the mass is in those particles. (iii) Under a wide range of conditions, dust torques could enable low-mass planetary cores formed in the inner disk to migrate outwards and act as the seed for massive planets at distances of tens of au, which could be responsible for the large-scale structures observed by ALMA.

## 7.2. Conclusion

Our most important conclusion is that, under a wide range of conditions that are usually assumed to hold when modeling planet formation processes, dust torques can have an important effect on the evolution of planetary embryos. This may well be an important fundamental piece missing in the puzzle of planet migration and formation (Morbidelli & Raymond 2016).

The detailed outcome when computing evolutionary tracks depends on the dust content and global evolution of the disk. However, it is clear that the fast inward migration of low-mass planetary embryos, known to affect gaseous disks, can be significantly alleviated as a natural consequence of the torques exerted by dust. As a result, the long-term orbital evolution of planetary embryos can differ substantially from those obtained in dust-free disks. Given the importance of the role of dust and planet migration in planet formation, we hope that our findings will motivate further studies of the processes involved to develop a more complete and coherent framework for making progress under more astrophysically realistic assumptions.

## Acknowledgments

We are grateful to the referee for a thoughtful report and useful suggestions that helped us improve the manuscript. O.M.G. is partially supported by PICT 2018-0934 from ANPCyT, Argentina. O.M.G. and M.M.M.B. are partially supported by PIP-2971 from CONICET (Argentina) and by PICT 2020-03316 from Agencia I + D + i (Argentina). O.M.G. acknowledges support by ANID,—Millennium Science Initiative Program—NCN19\_171. O.M.G. and M.M.M.B. also thank Juan Ignacio Rodriguez from IALP for the computation managing resources of the Grupo de Astrofísica Planetaria de La Plata. P.B.L. acknowledges support from FONDECYT project 1231205. M.E.P. gratefully acknowledges support from

the Independent Research Fund Denmark via grant No. DFF 8021-00400B and the Institute for Advanced Study, where part of this work was done.

## Appendix

### An Alternative Approach for Computing the Dust Torque

An alternative way of computing the dust torque from the hydrodynamical simulations of BL18 consists of assuming that the dust torque  $\Gamma_d$  is proportional to the gas torque  $\Gamma_g$  instead of the reference torque  $\Gamma_p$ , as is done in Section 2. Under this assumption, the dust torque becomes

$$\frac{\Gamma_d(r_p, \epsilon)}{\Gamma_g(r_p, \epsilon)} = \left(\frac{\epsilon}{\epsilon_0}\right) \times \frac{\Gamma_d(r_p, \epsilon_0)}{\Gamma_g(r_p, \epsilon_0)} = \left(\frac{\epsilon}{\epsilon_0}\right) \times \frac{\Gamma_d(r_0, \epsilon_0)}{\Gamma_g(r_0, \epsilon_0)}, \quad (15)$$

and thus

$$\begin{aligned} \Gamma_d(r_p, \epsilon) &= \left(\frac{\epsilon}{\epsilon_0}\right) \times \frac{\Gamma_d(r_0, \epsilon_0)}{\Gamma_g(r_0, \epsilon_0)} \times \Gamma_g(r_p, \epsilon) \\ &= \left(\frac{\epsilon}{\epsilon_0}\right) \times \left(\frac{\Gamma_d}{\Gamma_g}\right)_{\text{BLP18}} \times \Gamma_g(r_p, \epsilon) \\ &= \Phi(M_p, St, \epsilon) \times \Gamma_g(r_p, \epsilon), \end{aligned} \quad (16)$$

where  $\Gamma_g(r_0, \epsilon_0)$  is the gas torque from BLP18 computed adopting  $\epsilon_0 = 0.01$  and  $r_0 = 1$  au.<sup>12</sup> The ratio  $(\Gamma_d/\Gamma_g)_{\text{BLP18}}$  as a function of planet mass can be obtained<sup>13</sup> from the information provided in Table 1. Finally,  $\Gamma_g(r_p, \epsilon) = \Gamma_g(r_p)$  is computed for the corresponding gas disk model as described in Section 2.1.1.

In order to understand the impact of the model adopted for the dust torque, Figure 15 shows the normalized total torque for the case of a nonisothermal disk (see Section 4) when the dust torque is assumed to be proportional to the gas torque instead of the reference torque  $\Gamma_p$ , as was previously done using Equation (7). As in Figure 6, the left panel of Figure 15 shows the total torque over a planet in a dust-free disk, i.e.,  $\Gamma_{\text{tot}} = \Gamma_g$ . The following three panels show the total torque  $\Gamma_{\text{tot}} = \Gamma_g + \Gamma_d$  for the Stokes numbers  $St = \{0.1, 0.3, 1\}$ , considered to be constant throughout the disk, and assuming a gas-to-dust mass ratio  $\epsilon = 0.01$ .

The results shown in Figures 6 and 15 are qualitatively similar. The main difference is that in the latter, the transitions between negative and positive torques in dusty disks occur at a constant planet mass. This is because when the dust torque  $\Gamma_d$  is proportional to the gas torque  $\Gamma_g$ , they both have the same radial dependence. The fact that this boundary is independent of the planet mass can be seen by noting that the zero torque condition  $\Gamma_{\text{tot}} = 0$  corresponds to  $0 = (1 + \Phi(M_p, St, \epsilon)) \times \Gamma_g$ , which is satisfied by the same value of the planetary mass  $M_p$  regardless of the location of the planet,  $r_p$ .

We also note that in Figure 15, the total torque is lower compared to the total torque in Figure 6, where the color scale is strongly saturated (note that  $\Gamma_p$  is the same in both cases). This is also appreciable in Figure 16, which shows the normalized total torque at 1 au (considering that the dust torque  $\Gamma_d$  is given by Equation (16)) in a Stokes number–planet mass diagram as in Figure 5. We remark here that now the gas- and gravity-dominated regimes, where the dust torque generates a

<sup>12</sup> Note that the gas torque in BLP18 does not depend on the dust-to-gas mass ratio when this ratio is sufficiently small.

<sup>13</sup> For the values of the planet masses and Stokes numbers that are not tabulated, we use bilinear interpolation to obtain the ratio  $\Gamma_d/\Gamma_g$ .

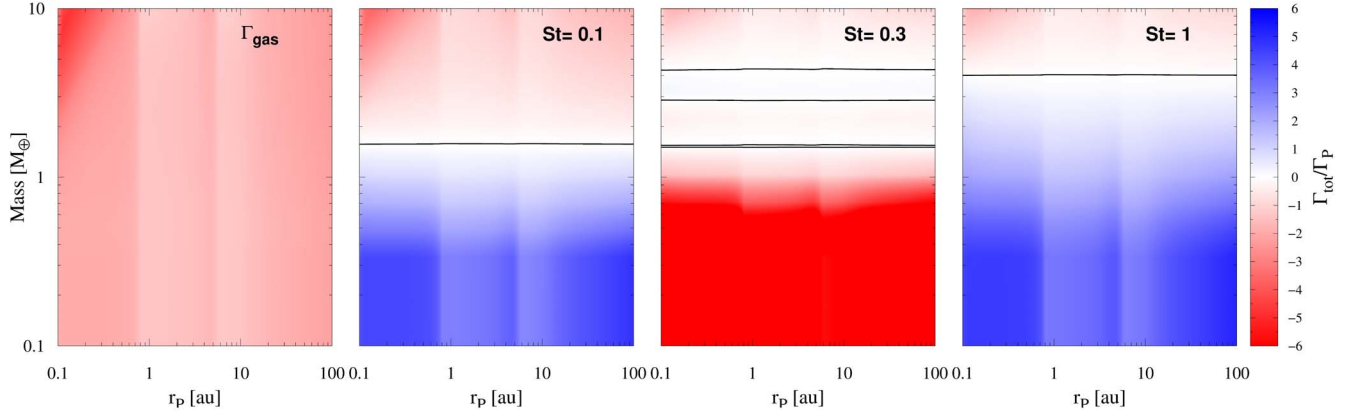


**Figure 15.** Same as Figure 6, but here the dust torque is computed using Equation (16) instead of Equation (7).

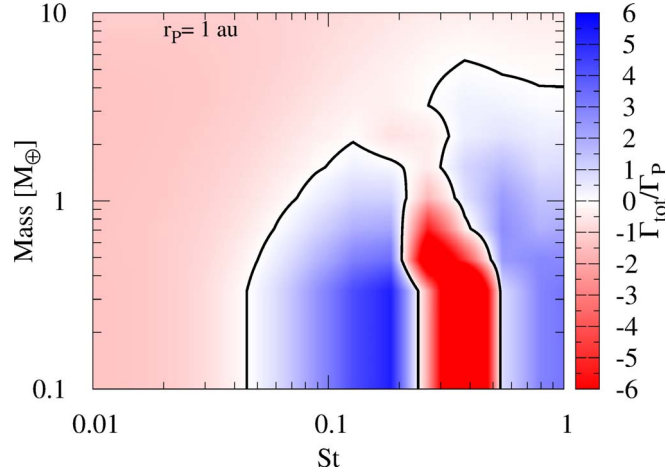


**Figure 16.** Same as Figure 5 but considering that the dust torque is obtained using Equation (16) instead of Equation (7).

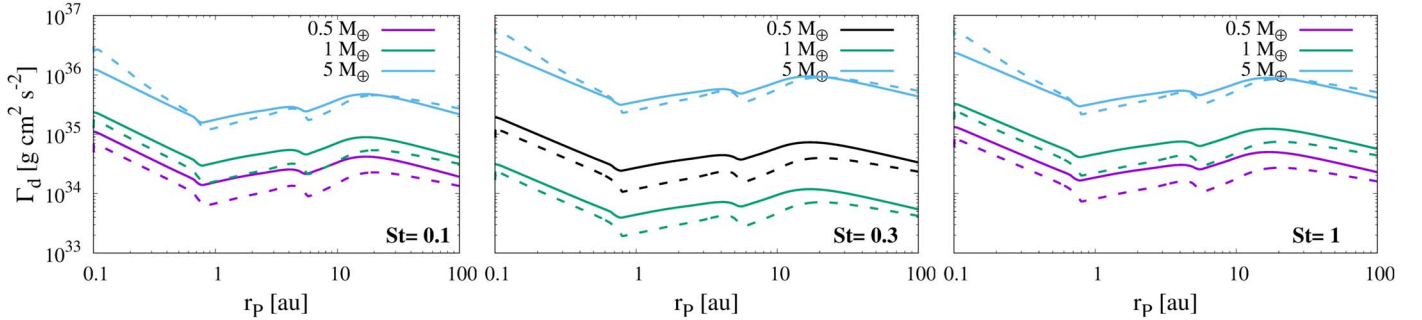


**Figure 17.** Radial profiles of the dust torque for different planet masses and Stokes numbers. The solid lines represent the dust torque computed via Equation (7), while the dashed lines correspond to the dust torque computed employing Equation (16). The black lines in the middle panel (the case of  $St = 0.3$ ) highlight the fact that for a planet mass of  $0.5 M_{\oplus}$ , the dust torques are negative in both approaches.

total positive torque, appear as disconnected regions in this diagram.

In order to assess the impact of the two approaches we outlined to compute the dust torque, we plot in Figure 17 the radial profile of the dust torque as obtained for three different planet masses,  $M_p = \{0.5, 1, 5\} M_{\oplus}$ , and three different Stokes numbers,  $St = \{0.1, 0.3, 1\}$ , from left to right. In spite of the fact that the magnitude of the dust torque (shown with solid lines) is generally slightly larger when using Equation (7), its radial dependence is qualitatively, and even roughly

quantitatively similar, independently of the approach used to compute it.

### ORCID iDs

Octavio M. Guilera <https://orcid.org/0000-0001-8577-9532>

Pablo Benitez-Llambay <https://orcid.org/0000-0002-3728-3329>

Marcelo M. Miller Bertolami <https://orcid.org/0000-0001-8031-1957>

Martin E. Pessah <https://orcid.org/0000-0001-8716-3563>

## References

- Andrews, S. M. 2020, *ARA&A*, 58, 483
- Baillié, K., Charnoz, S., & Pantin, E. 2016, *A&A*, 590, A60
- Baraffé, I., Homeier, D., Allard, F., & Chabrier, G. 2015, *A&A*, 577, A42
- Benítez-Llambay, P., Masset, F., Koenigsberger, G., & Szulágyi, J. 2015, *Natur*, 520, 63
- Benítez-Llambay, P., & Pessah, M. E. 2018, *ApJL*, 855, L28
- Birnstiel, T., Klahr, H., & Ercolano, B. 2012, *A&A*, 539, A148
- Bitsch, B., Johansen, A., Lambrechts, M., & Morbidelli, A. 2015, *A&A*, 575, A28
- Capobianco, C. C., Duncan, M., & Levison, H. F. 2011, *Icar*, 211, 819
- Chambers, J. 2021, *ApJ*, 914, 102
- Chen, J.-W., & Lin, M.-K. 2018, *MNRAS*, 478, 2737
- Chrenko, O., Brož, M., & Lambrechts, M. 2017, *A&A*, 606, A114
- Dittkrist, K.-M., Mordasini, C., Klahr, H., Alibert, Y., & Henning, T. 2014, *A&A*, 567, A121
- Dohnanyi, J. S. 1969, *JGR*, 74, 2531
- Drazkowska, J., & Alibert, Y. 2017, *A&A*, 608, A92
- Drazkowska, J., Alibert, Y., & Moore, B. 2016, *A&A*, 594, A105
- Drazkowska, J., Stammer, S. M., & Birnstiel, T. 2021, *A&A*, 647, A15
- Guilera, O. M., Cuello, N., Montesinos, M., et al. 2019, *MNRAS*, 486, 5690
- Guilera, O. M., Miller Bertolami, M. M., Masset, F., et al. 2021, *MNRAS*, 507, 3638
- Guilera, O. M., Miller Bertolami, M. M., & Ronco, M. P. 2017, *MNRAS Lett.*, 471, L16
- Guilera, O. M., & Sándor, Z. 2017, *A&A*, 604, A10
- Guilera, O. M., Sándor, Z., Ronco, M. P., Venturini, J., & Miller Bertolami, M. M. 2020, *A&A*, 642, A140
- Hartmann, L., Calvet, N., Gullbring, E., & D'Alessio, P. 1998, *ApJ*, 495, 385
- Hsieh, H.-F., & Lin, M.-K. 2020, *MNRAS*, 497, 2425
- Jiang, H., & Ormel, C. W. 2023, *MNRAS*, 518, 3877
- Jiménez, M. A., & Masset, F. S. 2017, *MNRAS*, 471, 4917
- Kanagawa, K. D. 2019, *ApJL*, 879, L19
- Kunitomo, M., Ida, S., Takeuchi, T., et al. 2021, *ApJ*, 909, 109
- Lambrechts, M., Johansen, A., & Morbidelli, A. 2014, *A&A*, 572, A35
- Lambrechts, M., Morbidelli, A., Jacobson, S. A., et al. 2019, *A&A*, 627, A83
- Masset, F. S. 2017, *MNRAS*, 472, 4204
- McNally, C. P., Nelson, R. P., Paardekooper, S.-J., & Benítez-Llambay, P. 2019, *MNRAS*, 484, 728
- Miguel, Y., Guilera, O. M., & Brunini, A. 2011, *MNRAS*, 412, 2113
- Miranda, R., & Rafikov, R. R. 2019, *ApJL*, 878, L9
- Morbidelli, A. 2020, *A&A*, 638, A1
- Morbidelli, A., & Raymond, S. N. 2016, *JGRE*, 121, 1962
- Ogihara, M., & Hori, Y. 2020, *ApJ*, 892, 124
- Paardekooper, S. J. 2014, *MNRAS*, 444, 2031
- Paardekooper, S.-J., Dong, R., Duffell, P., et al. 2022, arXiv:2203.09595
- Pierens, A., Lin, M. K., & Raymond, S. N. 2019, *MNRAS*, 488, 645
- Pinilla, P., Birnstiel, T., Ricci, L., et al. 2012, *A&A*, 538, A114
- Regály, Z. 2020, *MNRAS*, 497, 5540
- Ronco, M. P., Guilera, O. M., & de Elía, G. C. 2017, *MNRAS*, 471, 2753
- Schneider, A. D., & Bitsch, B. 2021, *A&A*, 654, A71
- Shakura, N. I., & Sunyaev, R. A. 1973, *A&A*, 24, 337
- Stammer, S. M., & Birnstiel, T. 2022, *ApJ*, 935, 35
- Tanaka, H., Takeuchi, T., & Ward, W. R. 2002, *ApJ*, 565, 1257
- Venturini, J., Guilera, O. M., Haldemann, J., Ronco, M. P., & Mordasini, C. 2020a, *A&A*, 643, L1
- Venturini, J., Guilera, O. M., Ronco, M. P., & Mordasini, C. 2020b, *A&A*, 644, A174
- Venturini, J., Ronco, M. P., & Guilera, O. M. 2020c, *SSRv*, 216, 86
- Voelkel, O., Klahr, H., Mordasini, C., & Emsenhuber, A. 2022, *A&A*, 666, A90
- Weber, P., Benítez-Llambay, P., Gressel, O., Krapp, L., & Pessah, M. E. 2018, *ApJ*, 854, 153
- Zhu, Z., Nelson, R. P., Dong, R., Espaillat, C., & Hartmann, L. 2012, *ApJ*, 755, 6